

Numerical Methods for Solving Nonlinearly Coupled Poisson Equations in Dual-Continuum Modeled Porous Electrodes

Yuhe Wang*

Min Wang^{†‡}Zhihang Xu[§]

Abstract

Porous electrodes are widely used in electrochemical systems, where accurately determining electric potentials, particularly overpotentials, is essential for understanding electrode behavior. At the macroscopic scale, we model porous electrodes using a dual-continuum formulation, in which the porous solid phase and the liquid electrolyte are represented as spatially superimposed continua. Determining the potential distributions then requires solving two Poisson equations that are nonlinearly coupled through Butler–Volmer kinetics under galvanostatic and potentiostatic operating modes. Under galvanostatic operation, these equations form an underconstrained singular system due to all-Neumann boundary conditions, posing numerical challenges. This paper systematically presents the numerical methods for solving the resulting nonlinearly coupled Poisson system in a dual-continuum framework, with a particular focus on galvanostatic solutions. We establish solution uniqueness in terms of the potential difference between the electrode and electrolyte (or overpotential), as well as the individual potentials up to a shared constant shift. To resolve this nonuniqueness, we introduce three numerical approaches: (1) Lagrange constrained method (LCM), (2) Dirichlet substitution method (DSM), and (3) global constraining method (GCM), which enables solving the overpotential without imposing an explicit system reference potential. Additionally, we provide both decoupled and fully coupled nonlinear solution strategies and evaluate their computational performance for homogeneous and heterogeneous conductivity fields. The presented modeling and numerical framework is general and can be applied to related underconstrained nonlinear systems.

Keywords: Porous Media, Poisson Equations, Nonlinear Coupling, Underconstrained PDE, Numerical Methods, Electric Potential Fields

1 Introduction

Porous electrodes play a crucial role in many electrochemical energy storage devices [1, 2]. Their large surface area and interconnected pore structures facilitate efficient electrochemical reactions and mass transport, both of which are critical to device performance. The efficiency of porous electrodes arises from the intricate interplay among ionic transport in the electrolyte, electronic conduction in the solid electrode phase, and electrochemical reactions occurring at the electrode-electrolyte interfaces within

*Institute for Scientific Computation, Texas A&M University, College Station, TX 77843, USA. yuhe.wang@tamu.edu

[†]Department of Mathematics, University of Houston, Houston, TX 77204, USA. mwang55@central.uh.edu

[‡]Corresponding author

[§]Department of Mathematics, University of Houston, Houston, TX 77204, USA. z xu29@central.uh.edu

the porous structure [3–6]. Understanding and optimizing these coupled processes are essential for advancing the design and performance of electrochemical energy storage devices, including batteries, flow cells, and supercapacitors [7, 8]. A key aspect of this is accurately modeling the electric potential fields in both the solid electrode and liquid electrolyte phases, as these fields dictate the localized distribution of electrochemical reaction rates and ultimately influence overall device efficiency [9, 10].

The continuum approach is commonly used for porous electrode modeling at the macroscopic level [11–13], where spatiotemporal variables are represented using “mean-field” approximations. In this framework, the electrode and electrolyte potential domains are superimposed, resulting in a system of coupled Poisson equations governed by charge conservation and electrochemical kinetics. The corresponding coupled potential field model for the porous electrode system is typically written in the following closure form [14–16]:

$$\nabla \cdot (-\sigma \nabla \phi_e) = \nabla \cdot \vec{j}_e \quad \text{in } \Omega_e, \quad (1a)$$

$$\nabla \cdot (-\kappa \nabla \phi_l) = \nabla \cdot \vec{j}_l \quad \text{in } \Omega_l, \quad (1b)$$

where the two Poisson equations are nonlinearly coupled through charge conservation and reaction kinetics [17, 18], given by:

$$\nabla \cdot \vec{j}_e = -\nabla \cdot \vec{j}_l = -sj, \quad (2a)$$

$$j = j_0 \left[\exp \left(\frac{(1-\alpha)F\eta}{RT} \right) - \exp \left(-\frac{\alpha F\eta}{RT} \right) \right], \quad (2b)$$

$$\eta = \phi_e - \phi_l - E_{eq}. \quad (2c)$$

The descriptions to the symbols in the above equations are summarized in Table 1. Notably, the right-hand sides of (1a) and (1b) have opposite signs, canceling each other when summed. Moreover, they exhibit a trigonometric hyperbolic dependence on the pair (ϕ_e, ϕ_l) , or more precisely, on their difference $\phi_e - \phi_l$. Furthermore, the current density j is negative for the reduction process and positive for the oxidation process.

Although it has not been framed this way in the relevant literature, (1a)–(1b) and (2a)–(2c) describe a dual-continuum approach in macroscopic modeling [19, 20]. This approach assumes that the two coupled dynamics are spatially superimposed, with their interaction governed by a pair of antisymmetric source/sink terms that enforce global conservation. By abstracting the system in this way, the dual-continuum approach effectively alleviates the need to resolve local porous geometry, significantly improving computational efficiency. This modeling strategy, along with its generalized versions, has been extensively studied in the porous media flow community as part of multiscale frameworks designed to upscale the coexistence of fast and slow fluid flow dynamics in complex media with well-distributed high- and low-conductivity regions [21–25].

In the context of porous electrodes, the dual-continuum setup considers the solid electrode and liquid electrolyte phases as coexisting everywhere and geometrically superimposed, such that $\Omega_e = \Omega_l$. The porous electrode system exhibits two distinct conductivity regimes in the sense that the solid phase has significantly higher electrical conductivity than the electrolyte phase. The right-hand sides of (1a) and (1b) form an antisymmetric pair, which can also be interpreted as internal or implicit boundary (interfacial) conditions governing the interaction between electrode and electrolyte dynamics. This

Table 1: Description of symbols in (1a)–(1b) and (2a)–(2c)

Symbol	Description	Unit
<i>Primary unknowns:</i>		
ϕ_e	Porous electrode potential	V
ϕ_l	Electrolyte potential	V
<i>Secondary unknowns:</i>		
\vec{j}_e	Current density in the porous electrode	A/m ²
\vec{j}_l	Current density in the electrolyte	A/m ²
j	Reaction current density	A/m ²
η	Overpotential	V
<i>Parameters:</i>		
σ	Electrical conductivity of the porous electrode	S/m
κ	Ionic conductivity of the electrolyte	S/m
α	Electron transfer coefficient	-
s	Specific surface area of the porous electrode	m ⁻¹
j_0	Exchange current density	A/m ²
F	Faraday constant, 96485	C/mol
R	Ideal gas constant, 8.314	J/(mol · K)
T	Operating temperature	K
E_{eq}	Equilibrium potential	V
Ω_e	The modeling domain of electrode	-
Ω_l	The modeling domain of electrolyte	-

coupling is generally described by the phenomenological Butler-Volmer equation [17,18,26], along with some forms of correction for surface species concentrations [27,28]. Unlike the porous media fluid flow applications, where such interfacial conditions are often approximated as pseudo-steady [21–25], the electrochemical system exhibits strong nonlinearity, following a hyperbolic semi-sinh dependence.

The numerical solution of (1a) and (1b) presents challenges primarily in two aspects. First, the right-hand side is highly nonlinear, exhibiting a hyperbolic dependence on the unknowns (ϕ_e and ϕ_l). Even a small variation in $(\phi_e - \phi_l)$ can lead to significant changes in the right-hand side, potentially causing numerical instability. Second, a major challenge arises from the boundary conditions, which are intricate due to the coupled nature of the system and are dictated by the operating mode of the electrochemical cell. Electrochemical cells are typically operated under either galvanostatic or potentiostatic control, with galvanostatic operation being more common [2,11]. Each mode determines the boundary conditions used in modeling. In galvanostatic operation, the current flux through the cell is fixed and externally controlled, allowing the potential to adjust dynamically in response to internal electrochemical reactions and mass transport. This applied current flux leads to an all-Neumann boundary setup for the two Poisson equations, rendering the system under-constrained and making standard numerical solution strategies unsuitable due to singularity issues. In contrast, under potentiostatic operation, the potential difference between the electrodes (typically between the working and reference electrodes) is maintained at a prescribed value, while the current adapts accordingly to accommodate reaction kinetics and transport processes. This results in a Dirichlet boundary condition

for the electrode potential, providing a much more well-posed setup for numerical solutions.

Most continuum-level porous-electrode studies rely on commercial solvers to compute galvanostatic responses of the coupled system and report simulation results under homogeneous conductivity fields [14, 15, 29–33]. These works typically present the governing equations and all-Neumann boundary conditions, but give little discussion of the numerical treatment needed to obtain a well-posed solution. As a result, the computational methodology is difficult to reproduce, assess, or transfer to heterogeneous settings and alternative numerical frameworks. This work is thus motivated to provide the explicit numerical schemes for the galvanostatic case and a basis for implementation and benchmarking beyond black-box solvers.

The main contributions of this paper are as follows: (1) we prove that, under galvanostatic conditions, the coupled system admit a unique solution in terms of $(\phi_e - \phi_l)$ and a unique pair of (ϕ_e, ϕ_l) , up to a shared constant shift in the solution space of ϕ_e and ϕ_l . (2) we provide two methods to eliminate this constant shift: a Lagrange-multiplier constraint derived from a unified energy functional, and a Gauss-theorem-based Dirichlet substitution. (3) we develop two nonlinear solution schemes for solving the galvanostatic problem: a decoupled approach and a fully coupled approach. (4) we demonstrate that, without introducing any additional reference potential, a solution can still be obtained using global constraining in a purely mathematical sense to address the singular system in the fully coupled scheme.

2 Mathematical Model

2.1 Governing Equations

We consider a symmetric single-electron redox reaction and set $\alpha = 0.5$ [11, 34]. We focus on reduction ($j < 0$) [2]. The methods in Sections 3 and 4 extend to oxidation, asymmetric α , and transient transport. With these assumptions, (1a)–(2c) reduce to

$$\nabla \cdot (-\sigma \nabla \phi_e) = -a \sinh(b\eta) \quad \text{in } \Omega_e, \quad (3a)$$

$$\nabla \cdot (-\kappa \nabla \phi_l) = a \sinh(b\eta) \quad \text{in } \Omega_l, \quad (3b)$$

where $\eta := \phi_e - \phi_l - E_{eq}$, $a = 2sj_0$, and $b = \frac{0.5F}{RT}$.

2.2 Model Geometry

The model geometry considered in this paper is illustrated in Figure 1. The domain representing a half-cell setup comprises a porous electrode positioned between a current collector on the left and a membrane separator on the right. The porous electrode is modeled as a composite material comprising a solid matrix (shown in gray) and pore spaces (shown in white), the latter being filled with electrolyte. The model extends over a width W in the x -direction and a height H in the y -direction, with the current collector and membrane separator defining the left and right boundaries, respectively. The entire system can be characterized by its dual-continuum nature, consisting of a solid electrode-continuum Ω_e and a liquid-continuum Ω_l that are spatially superimposed. In the following, when we use the symbol Ω , it denotes both the electrode and the electrolyte domains without explicitly distinguishing them. The redox reaction interface between these two continua is formed by the surface

of the pore space. It acts as an implicit internal interfacial boundary where electrochemical reactions occur. This dual-continuum configuration serves as the foundation for describing the coupled potential fields arising from electronic and ionic conduction.

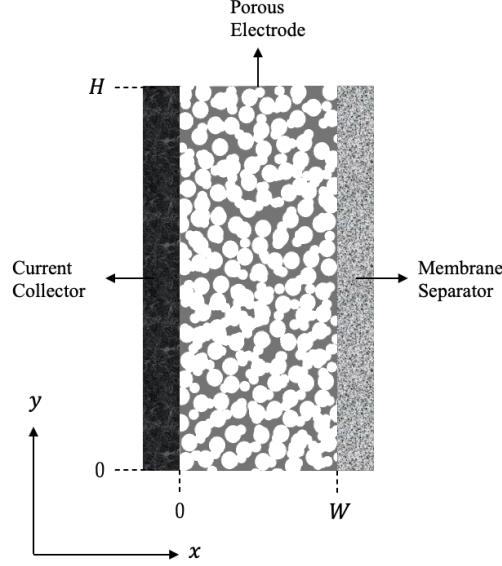


Figure 1: The half-cell porous electrode model geometry

2.3 Boundary Conditions

Here, we consider both the galvanostatic and potentiostatic operating conditions. We assume the boundaries consist entirely of either Dirichlet or Neumann conditions.

Galvanostatic. The left boundary $x = 0$ of Ω_e , attaching to the current collector, is subjected to a fixed current density applied through the external circuit. Since the membrane separator is not conductive to electrons, the right boundary $x = W$ of Ω_e is considered to have no electron current flux. Additionally, the top and bottom boundaries are assumed to be insulated to current flux. The boundary conditions for the porous electrode are:

$$\sigma \frac{\partial \phi_e}{\partial n} = \begin{cases} -j_{\text{applied}}, & \text{at } x = 0, \\ 0, & \text{at } x = W, y = 0, y = H, \end{cases} \quad (4)$$

where j_{applied} is the applied current density (A/m^2) and $\frac{\partial \phi_e}{\partial n}$ denotes the directional derivative in the outward normal to the boundary. For the electrolyte domain, its left boundary $x = 0$ does not support ionic conduction, resulting in no ionic current flux. Conversely, at its right boundary $x = W$ in contact with the membrane separator, there is supporting ionic flux between the positive and negative electrolyte regions. This ionic current flux balances the charge changes caused by electrochemical reactions and completes the internal current circuit. Under galvanostatic operation, the ionic current density at $x = W$ matches the current density applied to the electrode via the current collector. The

top and bottom boundaries are insulated with respect to ionic flux. We then have for the electrolyte:

$$\kappa \frac{\partial \phi_l}{\partial n} = \begin{cases} j_{\text{applied}}, & \text{at } x = W, \\ 0, & \text{at } x = 0, y = 0, y = H. \end{cases} \quad (5)$$

Here j_{applied} represents a non-negative value.

Potentiostatic. The left boundary $x = 0$ of Ω_e , attaching to the current collector, is set to an externally specified potential as a Dirichlet boundary condition. The remaining boundaries are the same as the galvanostatic case. Thus, we have:

$$\begin{cases} \phi_e = V_{\text{applied}}, & \text{at } x = 0, \\ \sigma \frac{\partial \phi_e}{\partial n} = 0, & \text{at } x = W, y = 0, y = H. \end{cases} \quad (6)$$

For the electrolyte domain, the boundaries at $x = 0$, $y = 0$, and $y = H$ of Ω_l remain under zero-flux conditions. However, the boundary at $x = W$ is not explicitly specified by the operating condition. We can impose either Dirichlet or Neumann boundaries there and then numerically sweep the respective boundary values when solving the system. Here we consider two cases:

$$\begin{cases} \phi_l = V_{\text{sweep}}, & \text{at } x = W, \\ \kappa \frac{\partial \phi_l}{\partial n} = 0, & \text{at } x = 0, y = 0, y = H, \end{cases} \quad (7)$$

$$\kappa \frac{\partial \phi_l}{\partial n} = \begin{cases} j_{\text{sweep}}, & \text{at } x = W, \\ 0, & \text{at } x = 0, y = 0, y = H, \end{cases} \quad (8)$$

where V_{sweep} and j_{sweep} are to be swept during solution.

3 Numerical Methods: Galvanostatic Solution

Due to the nonlinear source/sink terms in the coupled Poisson system, we need to devise proper iterative linearization schemes for the galvanostatic solution. However, the major challenge arises from the all-Neumann boundary conditions, which leads to non-uniqueness in the respective solution spaces of ϕ_e and ϕ_l . Such a situation results in a singular system matrix after discretization. In this section, we provide decoupled and coupled numerical schemes to address this issue.

3.1 Solution Existence and Uniqueness

Existence. The solution existence requires satisfying a compatibility condition based on Gauss's theorem, as shown in (9a) and (9b). In a physical sense, this requirement is interpreted as charge

conservation.

$$\int_{\Omega_e} (-f) d\Omega_e = - \int_{\partial\Omega_e} \sigma \frac{\partial\phi_e}{\partial n} dS_e, \quad (9a)$$

$$\int_{\Omega_l} f d\Omega_l = - \int_{\partial\Omega_l} \kappa \frac{\partial\phi_l}{\partial n} dS_l. \quad (9b)$$

Here, $f = a \sinh(b\eta)$, while $\Omega_{e/l}$ and $\partial\Omega_{e/l}$ represent the interior and boundary of the model domain $\bar{\Omega}_{e/l}$, respectively. $dS_{e/l}$ denotes a differential surface element on $\partial\Omega_{e/l}$.

Uniqueness. For this nonlinearly coupled all-Neumann system, the potentials are not individually unique. The solution set consists of pairs (ϕ_e, ϕ_l) that are unique up to a shared additive constant (see **SI.A**),

$$\{(\phi_e, \phi_l) \mid \phi_e = \phi_e^* + C, \phi_l = \phi_l^* + C, C \in \mathbb{R}\}, \quad (10)$$

where (ϕ_e^*, ϕ_l^*) is any particular solution pair satisfying (3a)–(3b) with boundary conditions (4)–(5). (10) immediately yields the unique potential difference,

$$\phi_e - \phi_l = \phi_e^* - \phi_l^*, \quad (11)$$

and explains why the galvanostatic case is numerically delicate: ϕ_e and ϕ_l can drift by a constant unless one additional reference value is imposed to remove the nullspace. In practice, this can be achieved by fixing $\phi_e(x^*)$ or $\phi_l(x^*)$ at an arbitrary location x^* . For instance, we ground a point in the electrode or the current collector boundary/near-boundary region). Then the remaining task is to enforce this reference consistently within the chosen nonlinear solution strategy; below we present two ways to impose such a fixed-location reference and give decoupled and fully coupled numerical schemes.

3.2 Constant Potential Referencing

Lagrange Constraint Method (LCM). To fix the constant-shift degree of freedom, we impose a fixed-location potential reference in Ω_e via Lagrange multipliers, while keeping the galvanostatic boundary conditions unchanged. Although the reference location and value are arbitrary, we set $\phi_e = 0$ at selected points near the left boundary of Ω_e as a physically motivated choice. For the coupled system, a unified energy functional yields (see **SI.B**) the augmented formulation with boundary conditions in (4)–(5):

$$\nabla \cdot (-\sigma \nabla \phi_e) + f + \sum_{i=1}^m \lambda_i \delta(x - x_i) = 0 \quad \text{in } \Omega_e, \quad (12a)$$

$$\nabla \cdot (-\kappa \nabla \phi_l) - f = 0 \quad \text{in } \Omega_l, \quad (12b)$$

$$\phi_e(x_i) - c_i = 0 \quad \text{for } i = 1, \dots, m, \quad (12c)$$

where $x_i \in \Omega_e$ specify the constraint locations $\{x_1, \dots, x_m\}$, $\delta(\cdot)$ denotes the Dirac delta, and λ_i are the associated Lagrange multipliers; we collect them as $\Lambda_e := \{\lambda_i\}_{i=1}^m$. Thus, $\phi_e(x_i)$ is pinned to c_i and serves as the reference for the coupled galvanostatic solution. An analogous construction applies

if the reference is imposed on ϕ_l . Other local constraint techniques include penalty terms [35] and direct matrix modification [36]: the former enforces the constraint only approximately and can be sensitive to its heuristic penalty parameter, while the latter enforces $\phi = C$ by replacing one row of the discrete system, thereby discarding the original governing equation at that location and potentially creating a local imbalance in the discrete flux/residual; In contrast, the Lagrange approach enforces the constraint exactly in a theoretically consistent manner, preserving the original PDE structure (see **SI.B**), but requiring a larger algebraic system.

Dirichlet Substitution Method (DSM). Recall Section 3.1. By Gauss’s theorem, a Poisson equation satisfies a global compatibility condition. The net boundary flux over $\partial\Omega$ equals the total source/sink over Ω . This holds for both Neumann and Dirichlet problems, since Dirichlet boundaries imply a flux even when it is not prescribed. Therefore, in the galvanostatic setup, we may replace one Neumann boundary by an arbitrary Dirichlet reference potential without changing the original coupled system, because the substituted boundary flux is still determined by the same global balance together with the remaining Neumann boundaries. For example, under the galvanostatic boundary conditions in (4)–(5), we may replace the electrode Neumann condition at $x = 0$ by an arbitrary Dirichlet reference $\phi_e|_{x=0} = \phi_{\text{ref}}$. The flux across the substituted boundary is not an additional free input; it is determined implicitly by the same global balance and therefore matches the flux that would arise in the original all-Neumann formulation. In particular,

$$\int_{\partial\Omega_{e,\mathcal{D}}|_{x=0}} \sigma \frac{\partial\phi_e}{\partial n} dS_e = - \int_{\Omega_e} (-f) d\Omega_e = \int_{\Omega_l} f d\Omega_l = - \int_{\partial\Omega_{l,\mathcal{D}}|_{x=w}} \kappa \frac{\partial\phi_l}{\partial n} dS_l, \quad (13)$$

where \mathcal{N} and \mathcal{D} denote the Neumann and Dirichlet portions of the boundary, respectively.

3.3 Nonlinear Solution Schemes

In addition to imposing a constant reference potential, it is essential to establish internal referencing between ϕ_e and ϕ_l during the nonlinear solution process. We consider both decoupled schemes, where the two equations are solved sequentially, and fully coupled schemes, where they are solved simultaneously.

3.3.1 Decoupled Scheme

We use a staggered decoupling scheme for the coupled system (3a)–(3b). At iteration $k + 1$, we update ϕ_e and ϕ_l sequentially. Each solve uses the latest available information from the other domain at iteration k . This turns the coupled problem into a sequence of independent subproblems. Table 2 summarizes the procedure. In (14a) and (14b), choosing $m = k$ gives a fully explicit scheme, whereas $m = k + 1$ requires an implicit solve. We use $m = k + 1$ because the explicit option is generally unstable for elliptic problems. Our stopping criterion is designed for the strong sensitivity of $\sinh(\eta)$ to changes in η , which provides a reliable convergence monitor. This decoupling raises two issues: the coupling between ϕ_e and ϕ_l is only weakly imposed through the source term f , since the sequential solves do not enforce a direct gridblock-wise referencing between the two potentials; and imposing a constant reference in Ω_e removes the singularity in (14a), but (14b) remains singular. To address both, we introduce an additional reference potential c_l in Ω_l . This resolves the singular matrix in (14b) and provides a cross-referencing mechanism within the sequential scheme. However, (10) shows that only one global reference is needed to isolate a unique solution pair, so c_l cannot be prescribed after Ω_e is

anchored. We therefore treat c_l as an unknown and determine it from a closure condition. We use the compatibility constraint, or charge conservation, in (9a)–(9b)). In practice, c_l can be found using a search algorithm. Below, we show that both LCM and DSM can be adapted to iteratively solve for c_l in a self-consistent manner.

Table 2: Decoupled nonlinear solution scheme

Step	Description
<i>Initialization</i>	Set the initial guess for the nonlinear term $f^0(\eta)$ using average local current density.
<i>Iteration</i>	1. Solve the following two Poisson equations sequentially: $\nabla \cdot (-\sigma \nabla \phi_e^{k+1}) = -f(\phi_e^m - \phi_l^k - E_{\text{eq}}), \quad (14a)$ $\nabla \cdot (-\kappa \nabla \phi_l^{k+1}) = f(\phi_e^k - \phi_l^m - E_{\text{eq}}). \quad (14b)$ subject to boundary conditions (4) and (5). k is the iteration index. 2. Update the nonlinear term to $f^{k+1} := f(\eta^{k+1})$ for convergence check letting $\eta^{k+1} = \phi_e^{k+1} - \phi_l^{k+1} - E_{\text{eq}}$. 3. Check convergence: If $\ f^{k+1} - f^k\ $ falls below a predefined threshold, proceed to output. Otherwise, continue the update.
<i>Output</i>	Return the converged ϕ_e and ϕ_l .

LCM Discretization. We first write the discretized form of (12a) – (12c), which reads

$$A_e \Phi_e + \Delta_e^T \Lambda_e = F_e, \quad (15a)$$

$$\Delta_e \Phi_e = C_e, \quad (15b)$$

where A_e is the system matrix, F_e is the discretized right-hand side vector, $\Phi_e := [\phi_1^{k+1}, \phi_2^{k+1}, \dots]^T$, Λ_e is the Lagrange multiplier vector, and $C_e := c_e \mathbf{1}_{n_c}$ is the reference potential vector, where $\mathbf{1}_{n_c} = [1, 1, \dots, 1]^T \in \mathbb{R}^{n_c}$ and n_c is the number of constrained gridblocks. The Neumann boundary condition information is incorporated A_e and F_e . Δ_e is a Dirac delta matrix with entries of 1 at the locations corresponding to the constraints, and 0 elsewhere. It projects the Λ_e and Φ_e vectors onto the indices of the constrained gridblocks. The matrix Δ_e has dimensions $n_c \times N$, where N is the total number of gridblocks. Each row of this sparse matrix corresponds to a constrained gridblocks. The corresponding discretization of Ω_l can be done in an analogous way. The resulting linear systems are:

$$\begin{bmatrix} A_e & \Delta_e^T \\ \Delta_e & 0 \end{bmatrix} \begin{bmatrix} \Phi_e \\ \Lambda_e \end{bmatrix}^{k+1} = \begin{bmatrix} F_e^{k/k+1} \\ C_e \end{bmatrix}, \quad (16a)$$

$$\begin{bmatrix} A_l & \Delta_l^T \\ \Delta_l & 0 \end{bmatrix} \begin{bmatrix} \Phi_l \\ \Lambda_l \end{bmatrix}^{k+1} = \begin{bmatrix} F_l^{k/k+1} \\ C_l^* \end{bmatrix}. \quad (16b)$$

where $C_l^* := c_l^* \mathbf{1}_{n_l}$ is an vector parametrized by an unknown c_l^* . The superscript $k/k+1$ indicates, for example, F_e is evaluated using $\phi_e^{k/k+1}$.

DSM Discretization. In this case, the discretization is simpler as c_e and c_l^* are imposed as constant Dirichlet boundaries at $x = 0$ and $x = W$. The resulting discretized system is given by:

$$A_e \Phi_e^{k+1} = F_e^{k/k+1} \quad \text{and} \quad A_l \Phi_l^{k+1} = F_l^{k/k+1} \quad (17)$$

where the corresponding Dirichlet boundaries are incorporated in (A_e, F_e) and (A_l, F_l) .

Unknown Reference Potential Search. We determine the unknown reference potential c_l^* by formulating an optimization problem to isolate its unique value that satisfies (9a) and (9b). Together with (13), we define the following objective function:

$$c_l^* = \arg \min_{c_l} \left\| \int_{\mathcal{B}} j_{\text{applied}} dS + \int_{\Omega} f(\cdot; c_l) d\Omega \right\|^2, \quad \mathcal{B} = \partial\Omega|_{x=0} \text{ or } \mathcal{B} = \partial\Omega|_{x=W}. \quad (18)$$

To solve this optimization problem, we employ a gradient descent approach with a line search mechanism [37] that dynamically adjusts the search step size (see **SI.C**). This method iteratively refines the reference potential with linear convergence. In Table 3, we outline the complete solution strategy. It incorporates the staggered iteration as an inner loop for solving the nonlinear Poisson equations sequentially, with either the LCM or DSM approach used to impose c_e and c_l^* . The combination of the outer search loop and the inner Picard iteration thus provides a way for obtaining galvanostatic solutions in a decoupled fashion while ensuring internal referencing between ϕ_e and ϕ_l . This approach can address the singularity issues and enforces charge conservation in a self-consistent manner.

Table 3: Galvanostatic solution strategy using decoupled scheme

Step	Description
<i>Initialization</i>	Set a initial reference potential c_l^* .
<i>Solve</i>	Refer to Table 2. Use LCM or DSM to solve the coupled nonlinear Poisson equations in a sequential fashion. Iterate until convergence or reaching stopping criteria.
<i>Optimization</i>	<ol style="list-style-type: none"> 1. Check convergence using (18): If the mismatch is below the prescribed tolerance, exit and output the solution ϕ_e and ϕ_l; otherwise, continue. 2. Compute the gradient of (18). 3. Perform line search to obtain an optimized step size. 4. Update c_l^* and rerun to solve the decoupled PDEs.
<i>Output</i>	Return the globally converged solution ϕ_e and ϕ_l .

3.3.2 Fully Coupled Scheme

A fully coupled formulation can enforce gridblock-wise cross-referencing between ϕ_e and ϕ_l , which removes the need to introduce and search for c_l^* . We can solve (3a)–(3b) simultaneously using a fully coupled Jacobian system, treating ϕ_e and ϕ_l implicitly in the nonlinear solve. In contrast to the decoupled scheme, which holds one field fixed while updating the other, the coupled Jacobian captures the cross-dependence of the two potentials and suppresses arbitrary constant shifts by enforcing internal referencing within the assembled system. We demonstrate both LCM and DSM to impose a constant

reference potential, and we also present a global constraining method that first computes the unique difference $\phi_e - \phi_l$ and then recovers ϕ_e and ϕ_l by post-processing under an arbitrary constant reference.

LCM Discretization. Discretizing **Eqs. (12a)–(12c)** gives:

$$Q_e^L = A_e \Phi_e - F_e + \Delta_e^T \Lambda_e, \quad (19a)$$

$$Q_l^L = A_l \Phi_l - F_l, \quad (19b)$$

$$G_e^L = \Delta_e \Phi_e - C_e. \quad (19c)$$

where F_e and F_l are the discrete forms of $-f$ and f , and the superscript L denotes Lagrange. Define the stacked residual and unknown as $R^L = [Q_e^L, Q_l^L, G_e^L]^T$ and $U^L = [\Phi_e, \Phi_l, \Lambda_e]^T$. The extended Jacobian system is

$$J^L \tau_U^L = -R^L, \quad J^L = \frac{\partial R^L}{\partial U^L}, \quad (20)$$

with update $U^{L,k+1} = U^{L,k} + \tau_U^L$. The Jacobian blocks are

$$\begin{aligned} \frac{\partial Q_e^L}{\partial \Phi_e} &= A_e - \frac{\partial F_e}{\partial \Phi_e}, & \frac{\partial Q_e^L}{\partial \Phi_l} &= -\frac{\partial F_e}{\partial \Phi_l}, & \frac{\partial Q_e^L}{\partial \Lambda_e} &= \Delta_e^T, \\ \frac{\partial Q_l^L}{\partial \Phi_e} &= -\frac{\partial F_l}{\partial \Phi_e}, & \frac{\partial Q_l^L}{\partial \Phi_l} &= A_l - \frac{\partial F_l}{\partial \Phi_l}, & \frac{\partial G_e^L}{\partial \Phi_e} &= \Delta_e, \end{aligned} \quad (21)$$

so that

$$\begin{bmatrix} A_e - \frac{\partial F_e}{\partial \Phi_e} & -\frac{\partial F_e}{\partial \Phi_l} & \Delta_e^T \\ -\frac{\partial F_l}{\partial \Phi_e} & A_l - \frac{\partial F_l}{\partial \Phi_l} & 0 \\ \Delta_e & 0 & 0 \end{bmatrix} \begin{bmatrix} \tau_{\Phi_e} \\ \tau_{\Phi_l} \\ \tau_{\Lambda_e} \end{bmatrix} = - \begin{bmatrix} Q_e^L \\ Q_l^L \\ G_e^L \end{bmatrix}. \quad (22)$$

Here G_e^L includes the imposed reference potential. The off-diagonal blocks $-\partial F_e/\partial \Phi_l$ and $-\partial F_l/\partial \Phi_e$ encode the cross-coupling between ϕ_e and ϕ_l , and the constraint rows remove the constant-shift nullspace, yielding a unique solution pair. It should be noted that, because the nonzero entries of Δ_e are 1, the extended system can be poorly scaled. We recommend scaling the Lagrange components separately to match the magnitude of the PDE blocks before assembling the final Jacobian.

DSM Discretization. The Jacobian system of DSM can be readily obtained by removing the Lagrange components and applying appropriate modifications to A_e and A_l , as well as $[Q_e]$ and $[Q_l]$, to accommodate the Dirichlet boundary conditions. The resulting Jacobian system is:

$$\begin{bmatrix} A_e^d - \frac{\partial F_e}{\partial \Phi_e} & -\frac{\partial F_e}{\partial \Phi_l} \\ -\frac{\partial F_l}{\partial \Phi_e} & A_l - \frac{\partial F_l}{\partial \Phi_l} \end{bmatrix} \begin{bmatrix} \tau_{\Phi_e} \\ \tau_{\Phi_l} \end{bmatrix} = \begin{bmatrix} Q_e^{d,r} \\ Q_l \end{bmatrix}. \quad (23)$$

where the subscript d denotes the incorporation of Dirichlet boundary substitutions, and the superscript r indicates the inclusion of the constant reference potential.

Global Constraining Method (GCM). By (10)–(11), the difference $\phi_e - \phi_l$ is unique. If ϕ_e and ϕ_l are cross-referenced gridblock-wise, the original Jacobian system,

$$\begin{bmatrix} A_e - \frac{\partial F_e}{\partial \Phi_e} & -\frac{\partial F_e}{\partial \Phi_l} \\ -\frac{\partial F_l}{\partial \Phi_e} & A_l - \frac{\partial F_l}{\partial \Phi_l} \end{bmatrix} \begin{bmatrix} \tau_{\Phi_e} \\ \tau_{\Phi_l} \end{bmatrix} = \begin{bmatrix} Q_e \\ Q_l \end{bmatrix}, \quad (24)$$

can be used to determine a unique update for $\phi_e - \phi_l$ even though the system has a shared constant-shift nullspace. We then can target to resolve the singularity by imposing global constraining measures that select a stable solution among the infinitely many. We consider three measures: (i) $\min_{\tau_{\Phi}} \|\tau_{\Phi}\|^2$, which selects the minimum-norm update and removes the free constant shift [38]; (ii) $\min_{\tau_{\Phi}} \|J\tau_{\Phi} - Q\|^2$, which seeks the least-squares residual solution and is commonly computed in a Krylov subspace [39]; and (iii) $\min_{\tau_{\Phi}} \|J\tau_{\Phi} - Q\|^2 + \lambda_T \|I\tau_{\Phi}\|^2$, which applies Tikhonov regularization [40] and uses λ_T to balance residual reduction and damping of τ_{Φ} . Here $\tau_{\Phi} = [\tau_{\Phi_e}, \tau_{\Phi_l}]^T$ and $Q = [Q_e, Q_l]^T$. In practice, the Moore–Penrose pseudoinverse minimizes $\|\tau_{\Phi}\|^2$ [41], MINRES minimizes $\|J\tau_{\Phi} - Q\|^2$ [42], and a least-squares solver with Tikhonov regularization such as LSMR/LSQR minimizes $\|J\tau_{\Phi} - Q\|^2 + \lambda_T \|I\tau_{\Phi}\|^2$ [43, 44]; we refer to the last option as LSTR (Least-Squares with Tikhonov Regularization). After obtaining any particular pair (ϕ_e^*, ϕ_l^*) , we recover the solution pair under an arbitrary constant reference C by a simple shift. If we reference at x_0 with $\phi_e(x_0) = C$, the shift is $\phi_e^*(x_0) - C$ and the final pair is

$$(\phi_e, \phi_l) = (\phi_e^*, \phi_l^*) - [\phi_e^*(x_0) - C]. \quad (25)$$

4 Numerical Methods: Potentiostatic Solution

For the sake of completeness, we briefly outline the numerical strategy for solving the potentiostatic system. In comparison with the galvanostatic condition, the potentiostatic solution is straightforward, as the coupled system includes a fixed Dirichlet boundary condition for Ω_e at $x = 0$. Unlike the galvanostatic case, where boundary conditions of Ω_l are explicitly specified at $x = 0$ and $x = W$, the boundary condition of Ω_l at $x = W$ in the potentiostatic system is not directly prescribed. Therefore, we consider two possible cases, as defined by (7) and (8): Dirichlet at $x = W$ and Neumann at $x = W$. However, the system admits multiple solutions depending on the specific assigned boundary values at $x = W$ for Ω_l , whether Dirichlet or Neumann. We thus can numerically sweep such boundary values to compute a series of different potentiostatic responses for both cases.

Dirichlet at $x = W$. This case is trivial as the coupled system is well-constrained without any solution ambiguity. We can solve the system using either decoupled or fully-coupled approaches by sweeping the value $V_{\text{sweep}} = \phi_l(x = W)$, provided that the sweeping boundary value remains within a physically meaningful and compatible range. For instance, in a charging process at the negative electrode, V_{sweep} should be larger than $V_{\text{applied}} = \phi_e(x = 0)$.

Neumann at $x = W$. The Ω_l setup here is analogous to the galvanostatic situation. Since $\phi_e(x = 0)$ is given, we can directly use (23) to solve this boundary flux sweeping problem. For the decoupled

Picard iteration approach, we may need to introduce an unknown reference potential to Ω_l using either the LCM or DSM method, and then iteratively determine this unknown along the way to obtain a self-consistent system solution pair (ϕ_e, ϕ_l) .

5 Examples and Analysis

To validate and analyze the introduced numerical methods, we consider examples based on the model shown in Figure 1. The examples model the charging process at a negative porous electrode, where the reduction reaction $\text{Ox}^{3+} + e^- \rightarrow \text{Red}^{2+}$ converts a trivalent species Ox^{3+} to a divalent species Red^{2+} via a single-electron transfer. Table 4 summarizes the physical and operational parameters. Here, σ is corrected using a constant porosity of 0.78 based on a solid electrode material conductivity of 1000 S/m. The electrolyte conductivity κ is computed from the concentrations of Ox^{3+} and Red^{2+} , set to 1053 mol/m^3 and 27 mol/m^3 , respectively, and is corrected using 0.78 porosity as well. The relevant correlations are available in [15, 16, 32].

Table 4: Physical and operational parameters used in the examples

Symbol	Description	Value
<i>Electrode Geometry:</i>		
W	Porous electrode width (m)	5×10^{-3}
H	Porous electrode height (m)	1×10^{-1}
L	Porous electrode length (m)	1×10^{-1}
<i>Physical Parameters:</i>		
σ	Electrical conductivity of the porous electrode (S/m)	103.1891
κ	Ionic conductivity of the electrolyte (S/m)	5.9514
s	Specific surface area of the porous electrode (m^{-1})	1.64×10^4
α	Electron transfer coefficient (-)	0.5
j_0	Exchange current density (A/m^2)	2.7657
E_{eq}	Equilibrium potential (V)	-0.1609
F	Faraday constant (C/mol)	96485
R	Ideal gas constant ($\text{J}/(\text{mol} \cdot \text{K})$)	8.314
T	Operating temperature (K)	298.15
<i>Operational Parameters:</i>		
I_{applied}	Applied galvanostatic current (A)	(0, 10]
V_{applied}	Applied potentiostatic electrode potential (V)	0
V_{sweep}	Sweeping potentiostatic electrolyte potential at $x = W$ (V)	[0.1, 0.5]
I_{sweep}	Sweeping potentiostatic current at $x = W$ (A)	(0, 10]

We focus on galvanostatic solutions, because the potentiostatic case uses standard numerical procedures. The main exception is when the boundary current is swept. In that setting, the problem can be viewed as a DSM-type variant of the galvanostatic solution. Aside from Section 5.1, the remaining examples and analyses concern galvanostatic solutions. All numerical solutions, except for the global constraining cases, use BICGSTAB with an ILU preconditioner.

5.1 Comparison with “Exact” Solutions

We compare the numerical solutions with their “exact” counterparts. We consider uniform σ and κ for analytical solutions in a one-dimensional setting. Thus, (3a) and (3b) become:

$$\frac{d^2\phi_e}{dx^2} = \frac{a}{\sigma} \sinh(b\eta), \quad (26a)$$

$$\frac{d^2\phi_l}{dx^2} = -\frac{a}{\kappa} \sinh(b\eta), \quad (26b)$$

where $a = 2sj_0$ and $b = \frac{0.5F}{RT}$. Subtracting (26b) from (26a) gives $\frac{d^2\phi_e}{dx^2} - \frac{d^2\phi_l}{dx^2} = \frac{d^2(\phi_e - \phi_l)}{dx^2} = \frac{d^2(\eta + E_{eq})}{dx^2} = \frac{d^2\eta}{dx^2}$, and thus $\frac{d^2\eta}{dx^2} = c \sinh(b\eta)$, where $c = \left(\frac{a}{\sigma} + \frac{a}{\kappa}\right)$. Using the First Integral Method [45], we obtain the “exact” solution in implicit form (see **SI.D**)

$$x = \int_{\eta_1}^{\eta} \frac{d\eta}{\sqrt{\frac{2c}{b} \cosh(b\eta) + q_1^2 - \frac{2c}{b} \cosh(b\eta_1)}}, \quad (27)$$

where $\eta_1 = \eta(0)$ and $q_1 = \left.\frac{d\eta}{dx}\right|_{x=0}$. (27) defines an implicit relation between x and $\eta(x)$. The integral is elliptic. It is often evaluated numerically. The parameters η_1 and q_1 are not directly specified, as discussed in Section 2. In practice, galvanostatic and potentiostatic setups more naturally provide either (η_1, η_2) or (q_1, q_2) , with $\eta_2 = \eta(W)$ and $q_2 = \left.\frac{d\eta}{dx}\right|_{x=W}$. We therefore use the shooting method [46]. It determines η_1 when (q_1, q_2) are known, or determines q_1 when (η_1, η_2) are known.

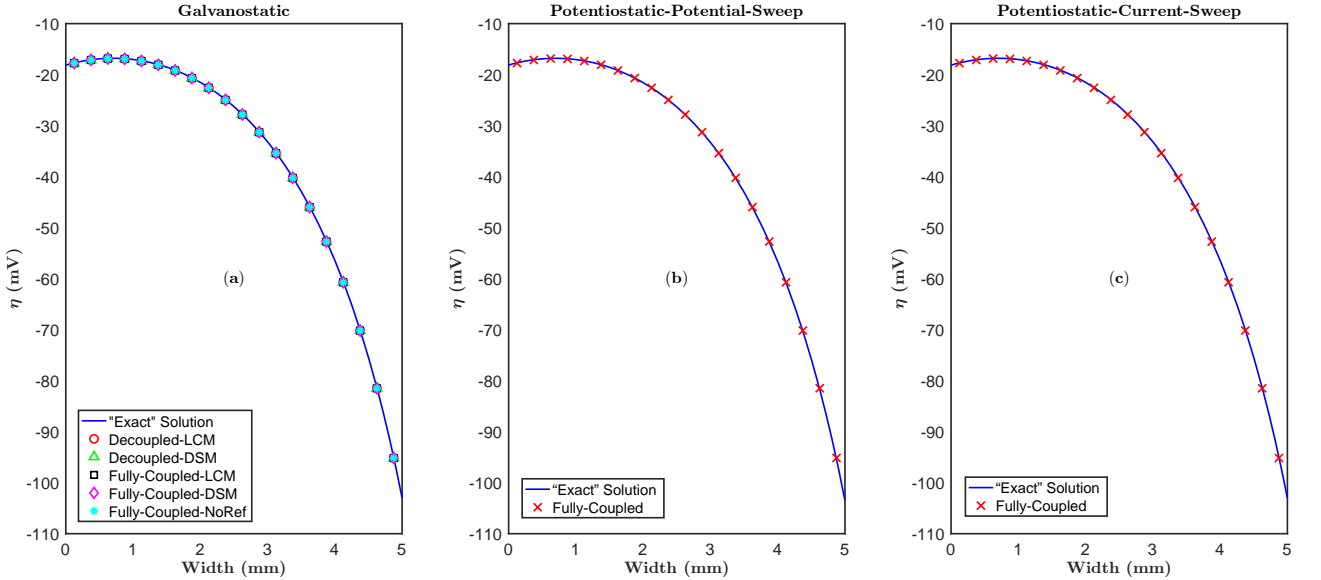


Figure 2: Numerical vs “exact” solutions. (a): Galvanostatic; (b): Potentiostatic with potential sweep; (c): Potentiostatic with current sweep

For the galvanostatic case, (4) and (5) give $q_1 = \frac{j_{\text{applied}}}{\sigma}$ and $q_2 = -\frac{j_{\text{applied}}}{\kappa}$. For the potentiostatic case, we consider two setups. One sweeps boundary current at $x = W$, so q_2 is known. In this case, charge conservation (13) yields $q_1 = -\frac{\kappa}{\sigma}q_2$. The other setup sweeps boundary potential at $x = W$.

Then we lack $(\phi_l(0), \phi_e(W))$ to compute (η_1, η_2) . We need the numerical solver in Section 4 to obtain these boundary values. Figure 2 compares the numerical solutions with the corresponding “exact” solutions. Figure 3 shows the L_2 and H_1 error reduction under mesh refinement. The numerical solutions match the “exact” profiles closely. The errors decrease quadratically with grid size. This confirms the accuracy and correctness of the proposed methods.

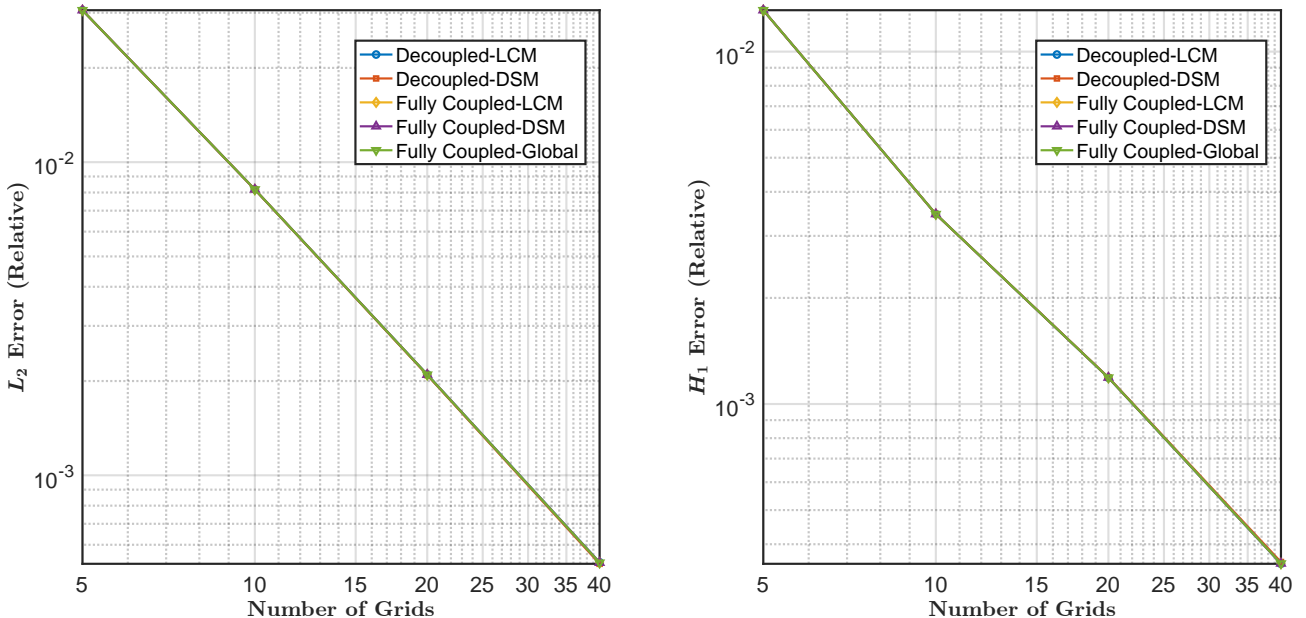


Figure 3: Error reduction (L_2 , H_1)

5.2 Objective Function for Finding the Electrolyte Reference Potential

As mentioned in Section 3, in a decoupled scheme the reference potential in Ω_l must be determined self-consistently during the solution process. We treat this as a search problem. The search is guided by the objective function in (18), which enforces compatibility between the boundary flux and the sink/source term. No simple analytical expression is available, so we approximate its discrete realization numerically by sampling the parameter space of the electrolyte reference potential. Figure 4 shows the objective function for $j_{\text{applied}} = 100 \text{ A/m}^2$. Extensive sampling over different j_{applied} values indicates a consistent piecewise-like trend. The function is flat for smaller reference potentials on the left of the minimum. It rises sharply after the minimum, indicating strong sensitivity to the reference potential. Right-side deviations lead to amplified discrepancies. The “V”-like shape near the minimum suggests that quadratic methods such as Newton’s method may be unsuitable, since second-derivative information is unlikely to be helpful there. Gradient descent may also struggle near the tip and can oscillate without proper step-size adaptation. A carefully designed step-size adjustment strategy is beneficial to avoid such issues. Alternatively, derivative-free optimization methods, such as Golden-section Search [47], may also perform well for this type of objective function.

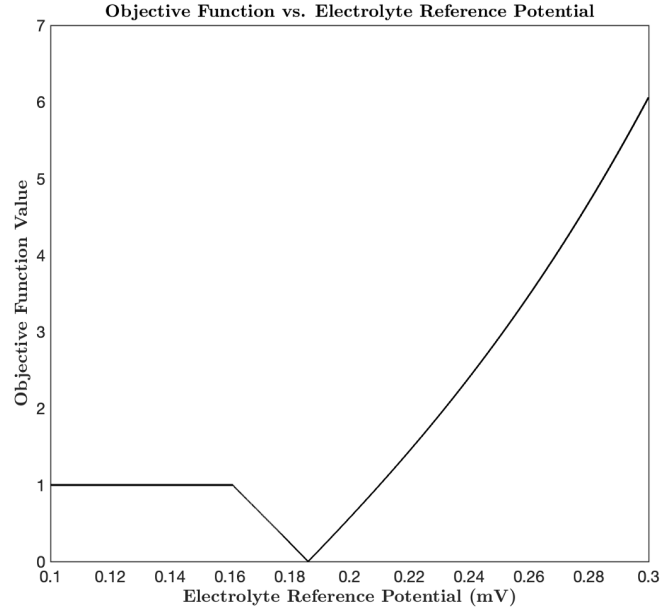


Figure 4: Objective function

5.3 Homogeneous vs. Heterogeneous

The potential and local current density distributions for homogeneous and heterogeneous conductivity fields are illustrated in Figures 5, 7, and 9. The corresponding bimodal and channalized conductivity fields are shown in Figures 6 and 8. Since the results obtained from different methods are very close, we present only the galvanostatic results obtained using fully coupled LCM scheme for the case of $j_{\text{applied}} = 1000 \text{ A/m}^2$. The computational grid is structured with dimension of 50×50 .

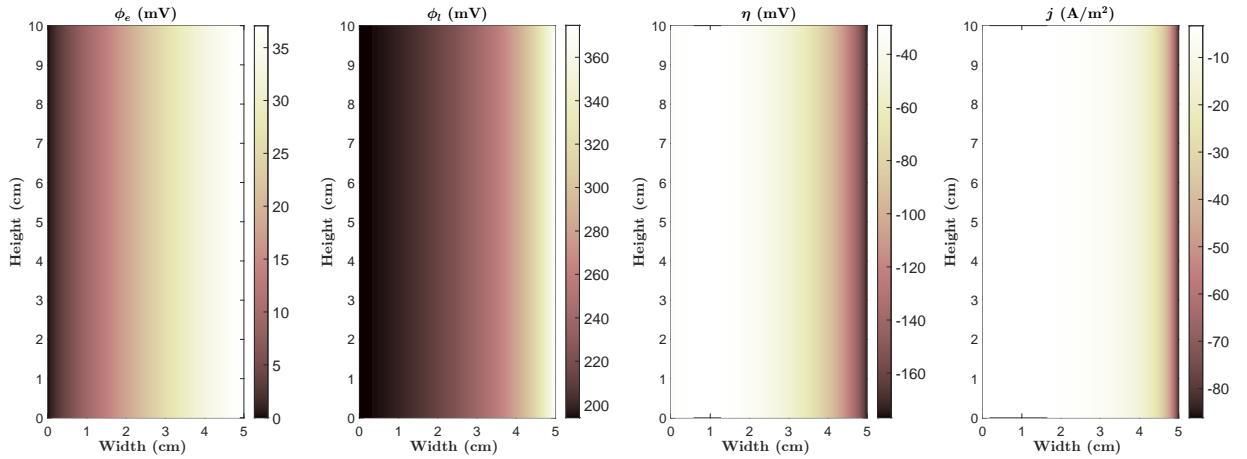


Figure 5: Potential (ϕ_e , ϕ_l , η) and local current density distributions (j) [Galvanostatic, $j_{\text{applied}} = 1000 \text{ A/m}^2$, homogeneous σ and κ , x-axis is scaled by 10 times]

In the homogeneous case, ϕ_e , ϕ_l , η , and j vary smoothly. ϕ_l is much larger than ϕ_e because σ is about

17 times larger than κ , leading to a larger potential drop in the electrolyte domain. η is smallest near the current collector ($x = 0$) and largest near the separator ($x = W$), confirming reaction dominance near the separator. The current density j is strongly localized near the separator, driven by the electrolyte potential drop. The patterns match physical expectations and validate the solver.

For heterogeneous tests, we use randomized bimodal conductivity fields for σ and κ based on a bimodal porosity field with $\epsilon_{\text{low}} = 0.2$ and $\epsilon_{\text{high}} = 0.8$. Figure 6 shows one realization, and Figure 7 shows the resulting η and j fields. Compared with the homogeneous case, the contours become irregular due to the bimodal structure of σ and κ . Reaction localization remains near the separator (right boundary), where electrolyte-dominated transport yields higher overpotentials. The jagged features in j indicate current crowding, highlighting the impact of heterogeneity and connectivity on charge transport efficiency. Figure 9 shows the corresponding η and j distributions for the channelized conductivity case. The plots show localized regions of intensified overpotential and current density induced by channel connectivity. Together with the bimodal case, these results demonstrate that the proposed numerical methods can handle heterogeneous conductivity fields.

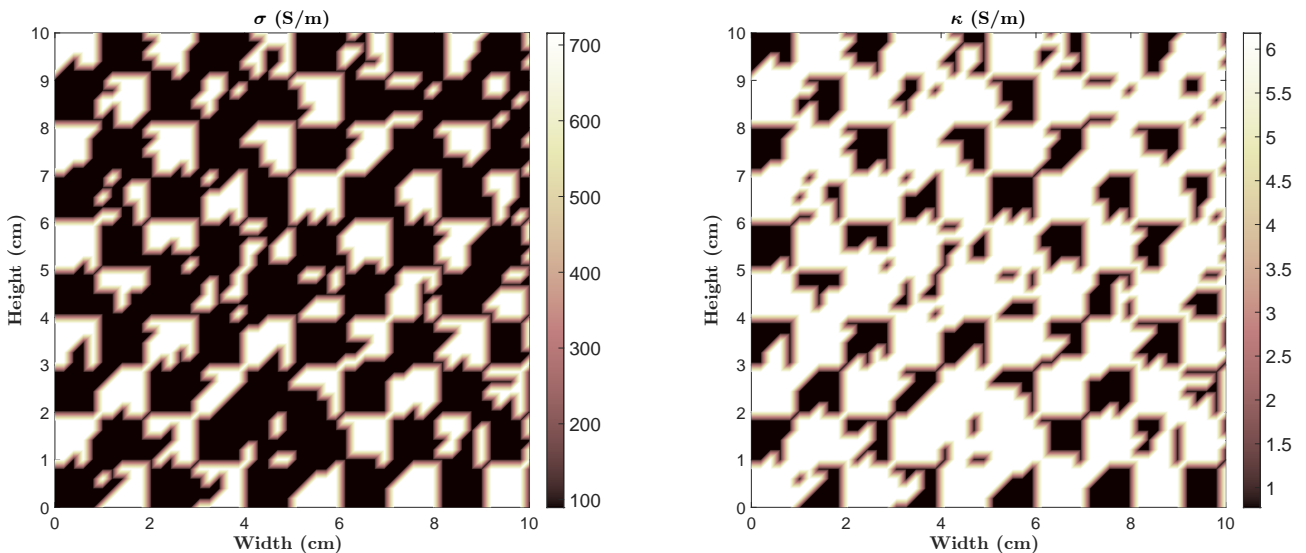


Figure 6: Bimodal porous electrode conductivity (σ) field and electrolyte conductivity (κ) field [x-axis is scaled by 20 times]

5.4 Decoupled vs. Fully Coupled

As described in Section 3.3.1, the decoupled scheme requires an outer search for the electrolyte reference potential c_l to maintain self-consistency with the coupled dynamics. Figure 10 shows that refining the grid does not change the convergence behavior of the c_l search. The search iteration count is approximately independent of N for both LCM and DSM. In these runs, LCM typically uses about 20% fewer search iterations than DSM. The drawback of the decoupled scheme is the added computational cost of this search. Each update of c_l requires multiple line-search iterations, and the two Poisson equations are solved two times per line-search iteration [37]. Each sequential solve also requires multiple nonlinear iterations. The linear systems solved in the decoupled scheme are smaller, with each system about half the size of the fully coupled system. However, the outer search repeats

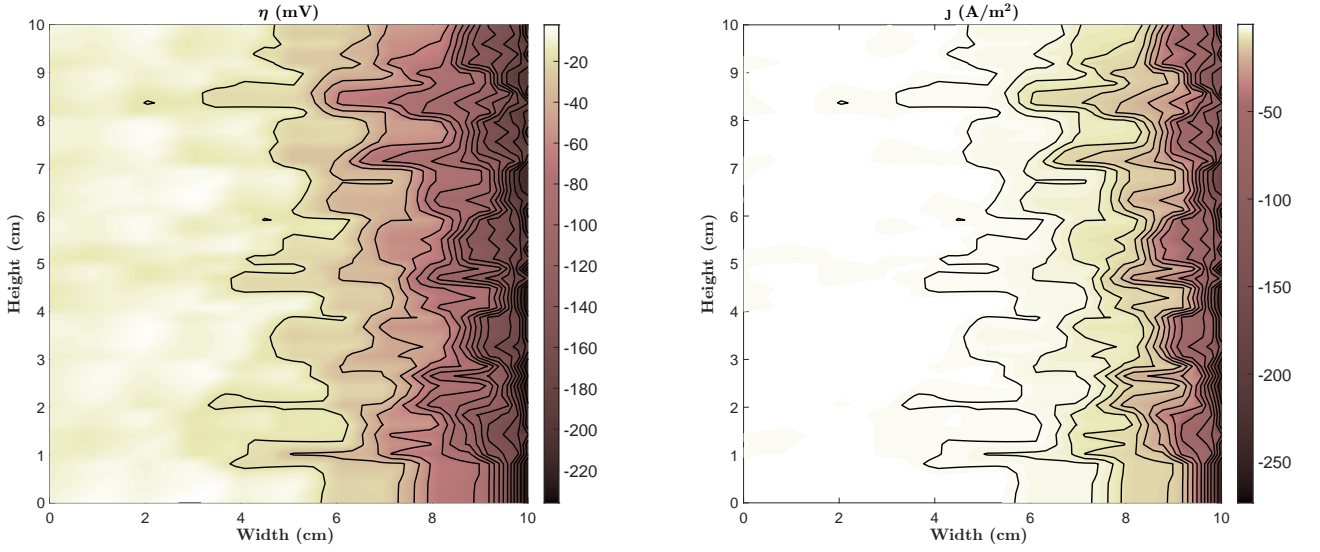


Figure 7: Overpotential (η) field and local current density (j) field of the bimodal conductivity case [$j_{\text{applied}} = 1000 \text{ A/m}^2$, x-axis is scaled by 20 times]

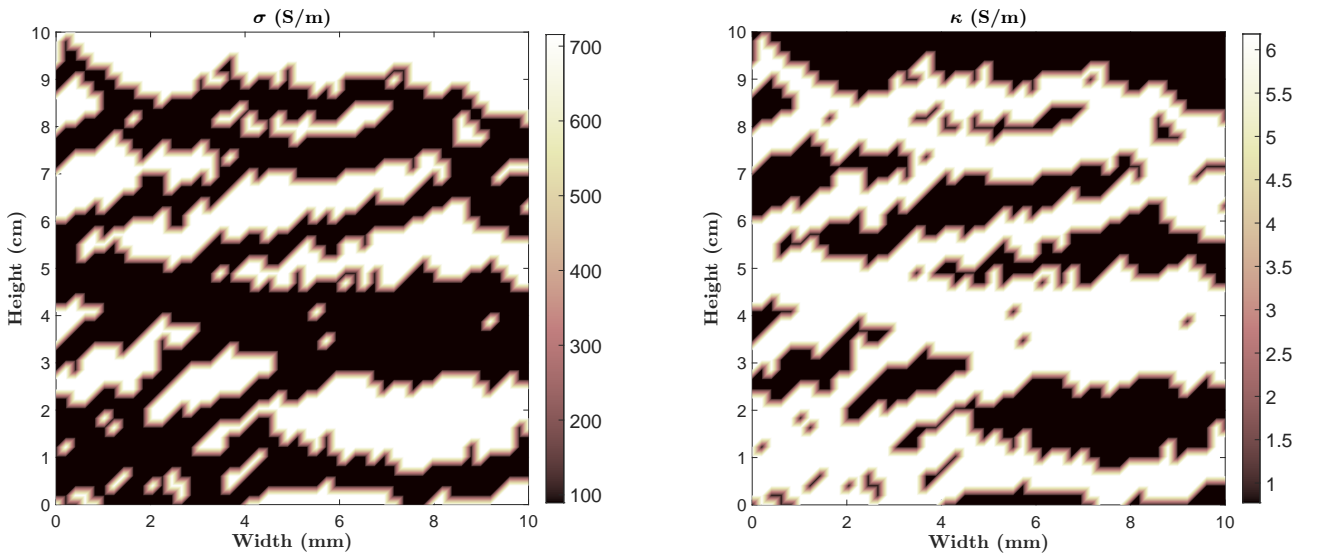


Figure 8: Channelized porous electrode conductivity (σ) field and electrolyte conductivity (κ) field [x-axis is scaled by 20]

these solves many times and can introduce an overhead of up to hundreds of times the cost of the fully coupled approach. Therefore, despite its simpler implementation, the decoupled scheme is not practical due to its high computational expense. In contrast, the fully coupled scheme solves the two Poisson equations only once. Figure 11 shows strong scalability for the fully coupled schemes with LCM and DSM. In these runs, DSM outperforms LCM for the homogeneous case and performs roughly the same as LCM for the heterogeneous case.

It should be noted that, for the decoupled solution, a full nonlinear iteration is not necessary, since

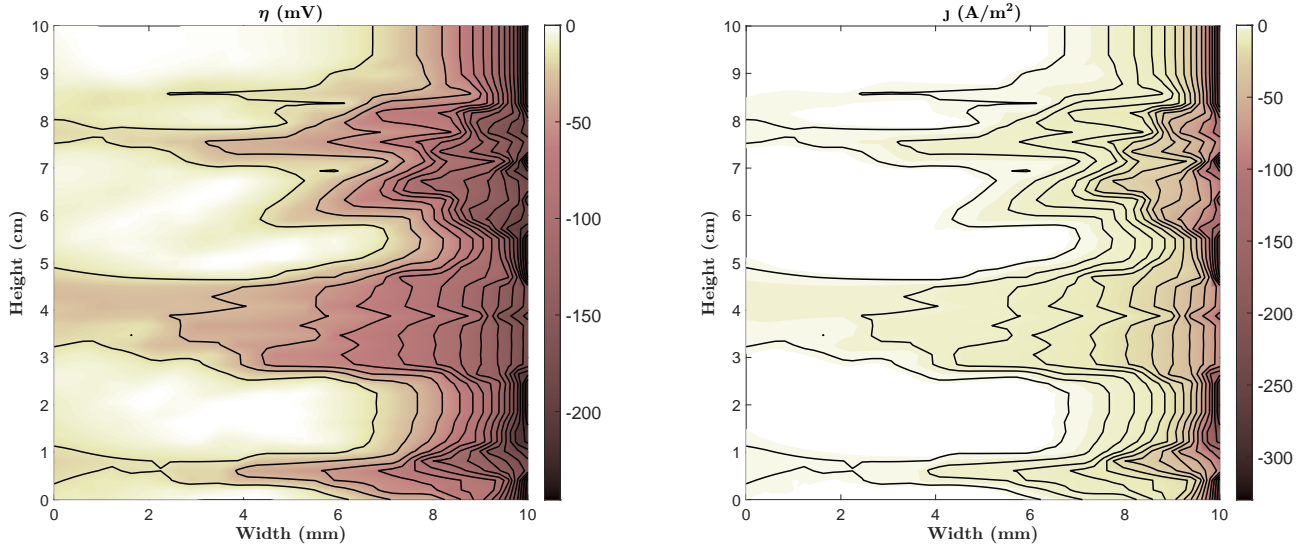


Figure 9: Overpotential (η) field and local current density (j) field of the channelized conductivity case [$j_{\text{applied}} = 1000 \text{ A/m}^2$, x-axis is scaled by 20]

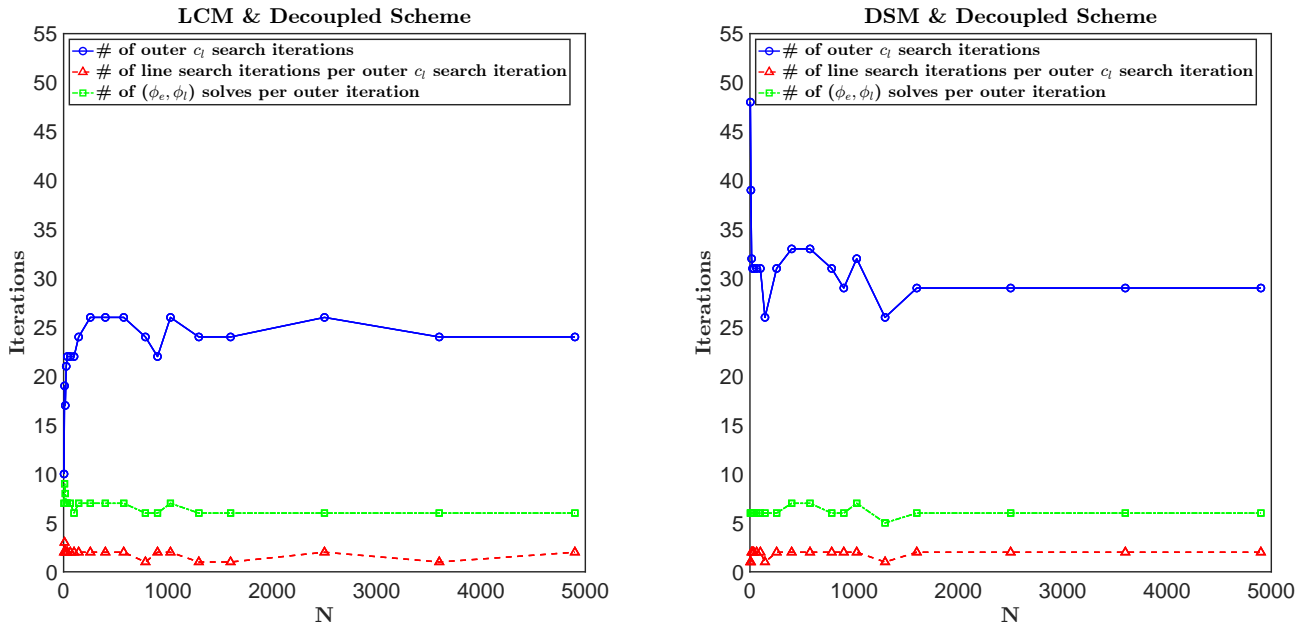


Figure 10: Iteration performance of the decoupled Scheme using LCM and DSM ($j_{\text{applied}} = 500 \text{ A/m}^2$, N is the size of Jacobian Matrix. The global residual tolerance is 1×10^{-6})

the outer search only needs an estimate of the search gradient. We therefore perform one nonlinear iteration per (ϕ_e, ϕ_l) solve, and the final solution is identical to runs with full iterations. Nevertheless, as long as such searching is used, the fully coupled scheme remains more attractive. The Jacobian-based iterations are sensitive to the initialization of (ϕ_e, ϕ_l) . The initial values affect the residual vector and the derivative terms in the Jacobian. These terms include highly nonlinear exponential

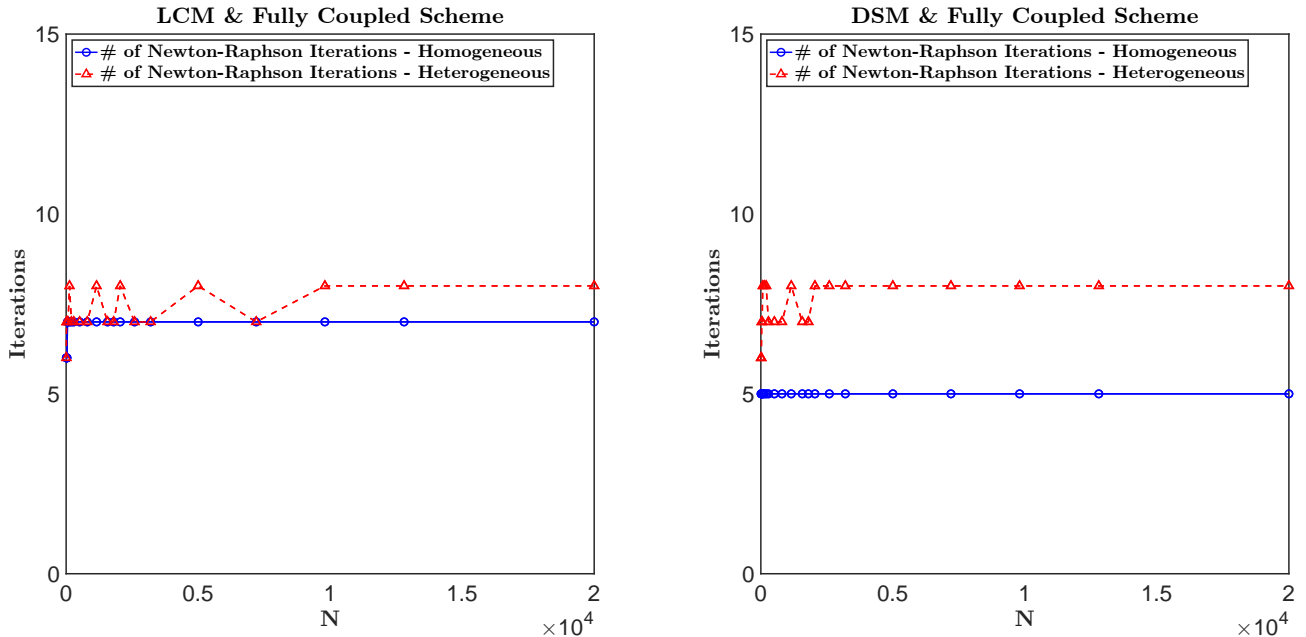


Figure 11: Iteration performance of the fully coupled scheme using LCM and DSM ($j_{\text{applied}} = 500 \text{ A/m}^2$, N is the size of Jacobian Matrix. The global residual tolerance is 1×10^{-6} . The heterogeneity is the bimodal case)

functions and can become extremely large in magnitude, which may lead to divergence. For stability, we recommend initializing $\phi_e = \phi_l = 0$. Alternatively, set $\phi_e = 0$ and $\phi_l = -E_{eq}$. LCM and DSM show similar convergence in our tests, suggesting that DSM may be preferable. LCM adds one internal constant-potential constraint, so $\text{size}(J^L) \approx \text{size}(J)$. However, it can produce a poorly scaled J^L , which may require special rescaling to reduce its condition number and can increase the number of linear solver iterations.

5.5 LCM/DSM vs. GCM

To assess the fully coupled scheme with GCM, we consider cases without imposing an explicit constant reference potential and report the convergence behavior for MINRES and LSTR in Figure 12. We do not include the Moore–Penrose pseudoinverse, because its $\mathcal{O}(N^3)$ cost can quickly exhaust computational resources. For the homogeneous case, MINRES and LSTR show identical performance, and they are comparable to the LCM/DSM results in Figure 11. For the heterogeneous case, MINRES struggles to reach the prescribed tolerance 1×10^{-6} , although the outer nonlinear iterations still converge. In contrast, LSTR performs well for the heterogeneous case. Therefore, LSTR is preferable to MINRES. We notice that inexact linear solves can still support global nonlinear convergence, as long as the linear residual reaches about 10^{-2} – 10^{-3} . This motivates iterative solvers with moderate accuracy for large-scale problems. However, inexact linear solves can degrade nonlinear convergence from quadratic to linear and may introduce mild oscillations.

To improve MINRES, we apply preconditioning. The Jacobian J is singular with $\text{rank} = N - 1$ and

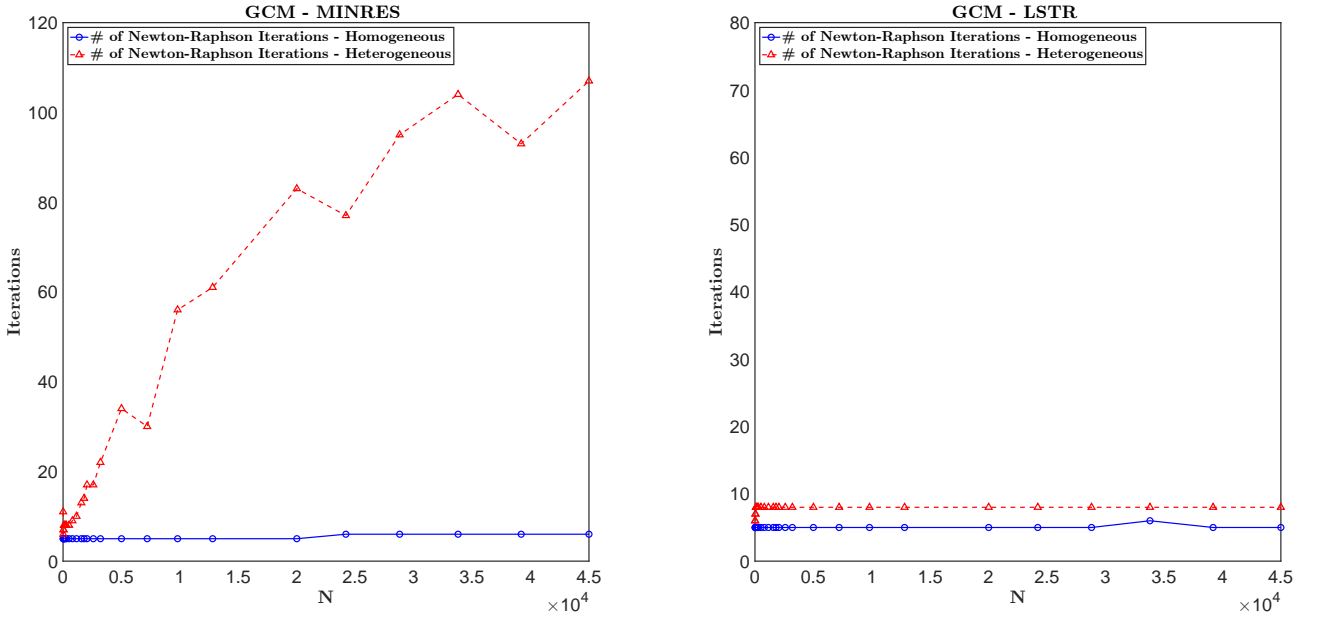


Figure 12: Iteration performance of the fully coupled scheme using MINRES and LSTR ($j_{\text{applied}} = 500 \text{ A/m}^2$, N is the size of the Jacobian matrix, global residual tolerance 1×10^{-6} , heterogeneity is the bimodal case).

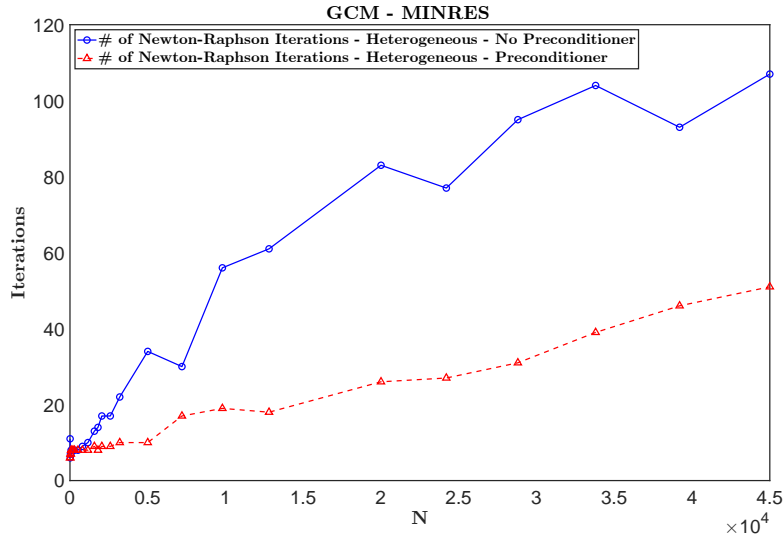


Figure 13: Iteration performance of the fully coupled scheme using MINRES with preconditioning ($j_{\text{applied}} = 500 \text{ A/m}^2$. N represents the size of the Jacobian matrix. The global residual tolerance is 1×10^{-6} . The heterogeneity is the bimodal case)

has a one-dimensional null space. We use the augmented system

$$J_{\text{aug}} = \begin{bmatrix} J & \lambda I \\ \lambda I & I \end{bmatrix}, \quad (28)$$

where λ is a regularization parameter, typically in 10^{-6} – 10^{-2} . Equation (28) shifts the singular values

away from zero and reduces the condition number. The matrix J_{aug} is twice the size of J , which can add considerable computational cost. To reduce this overhead, we use the Schur complement and obtain the reduced operator $J - \lambda^2 I$. Figure 13 shows that this preconditioning reduces the iteration count. The iteration count is still higher than LSTR. It also increases with N .

It should be noted that, for homogeneous conductivity fields, GCM with MINRES or LSTR is a viable approach, as it avoids the need to impose explicit potential references during the solve; the pair (ϕ_e, ϕ_l) is then recovered via the postprocessing shift in Eq. (25). For heterogeneous cases, the computational cost can be substantially higher than that of LCM/DSM when MINRES is used, and remains elevated with LSTR as well. Nevertheless, the key point is that galvanostatic solutions for $\phi_e - \phi_l$ or η can be obtained without specifying any explicit potential reference.

6 Conclusions

This work systematically provides the numerical methods for solving the nonlinearly coupled Poisson equations in dual-continuum modeled porous-electrode systems. Under galvanostatic conditions, we show that the system is uniquely determined in terms of the potential difference $\phi_e - \phi_l$ (or η), while ϕ_e and ϕ_l share a free additive constant, which makes the discrete system underconstrained and singular. To address this, we present three strategies: LCM, DSM, and GCM. LCM is based on Dirichlet’s principle and a Lagrange-multiplier constraint derived from a unified energy functional for the coupled Poisson dynamics. DSM follows from Gauss’s theorem. LCM and DSM impose an explicit reference potential, whereas GCM solves for $\phi_e - \phi_l$ (or η) without specifying a reference.

We also present decoupled and fully coupled nonlinear solution schemes. The fully coupled scheme is more efficient and robust, because the decoupled scheme requires an outer search for a reference potential to maintain self-consistency. In homogeneous cases, LCM, DSM, and GCM yield comparable performance. In heterogeneous cases, GCM can struggle with MINRES, even with preconditioning, while GCM with LSTR remains stable and efficient. Numerical results validate the methods across multiple conductivity fields and operating conditions, including underconstrained singularities, nonlinear source/sink coupling, and heterogeneity. The provided numerical framework is not restricted to 2D setting. It can be extended to 3D and to more general multicontinuum advection–diffusion–reaction models that fully couple species transport with electrochemical kinetics. We view these extensions as future directions to further the endeavor in multiphysics porous-electrode modeling.

Data and Code Availability

The code and data used in this study are available in the GitHub repository https://github.com/harrywang1129/porous_electrode_solver.

References

- [1] S. Santhanagopalan and R.E. White. Electrodes — porous electrodes. In Jürgen Garche, editor, *Encyclopedia of Electrochemical Power Sources*, pages 110–120. Elsevier, Amsterdam, 2009.

- [2] John Newman and Nitash P Balsara. *Electrochemical systems*. John Wiley & Sons, 2021.
- [3] Richard Alkire and Brian Gracon. Flow-through porous electrodes. *Journal of the Electrochemical Society*, 122(12):1594, 1975.
- [4] Zhenghui Pan, Jie Yang, Junhua Kong, Xian Jun Loh, John Wang, and Zhaolin Liu. “Porous and yet dense” electrodes for high-volumetric-performance electrochemical capacitors: Principles, advances, and challenges. *Advanced Science*, 9(4):2103953, 2022.
- [5] Hamid Hamed, Lowie Henderick, Behnam Ghalami Choobar, Jan D’Haen, Christophe Detavernier, An Hardy, and Mohammadhosein Safari. A limitation map of performance for porous electrodes in lithium-ion batteries. *Iscience*, 24(12), 2021.
- [6] Deyang Qu. Fundamental principals of battery design: Porous electrodes. In *AIP Conference Proceedings*, volume 1597, pages 14–25. American Institute of Physics, 2014.
- [7] Raymond B Smith and Martin Z Bazant. Multiphase porous electrode theory. *Journal of The Electrochemical Society*, 164(11):E3291, 2017.
- [8] Duo Zhang, Antoni Forner-Cuenca, Oluwadamilola O Taiwo, Vladimir Yufit, Fikile R Brushett, Nigel P Brandon, Sai Gu, and Qiong Cai. Understanding the role of the porous electrode microstructure in redox flow battery performance using an experimentally validated 3d pore-scale lattice boltzmann model. *Journal of Power Sources*, 447:227249, 2020.
- [9] John Newman and William Tiedemann. Porous-electrode theory with battery applications. *AIChE Journal*, 21(1):25–41, 1975.
- [10] Kiana Amini, Amin Sadeghi, Mark Pritzker, and Jeff Gostick. Porous electrodes in redox flow batteries. In Luisa F. Cabeza, editor, *Encyclopedia of Energy Storage*, pages 466–479. Elsevier, Oxford, 2022.
- [11] Allen J Bard, Larry R Faulkner, and Henry S White. *Electrochemical methods: fundamentals and applications*. John Wiley & Sons, 2022.
- [12] Justin C Bui, Eric W Lees, Lalit M Pant, Iryna V Zenyuk, Alexis T Bell, and Adam Z Weber. Continuum modeling of porous electrodes for electrochemical synthesis. *Chemical reviews*, 122(12):11022–11084, 2022.
- [13] Jakub K Włodarczyk, Gaël Mourouga, Roman P Schärer, and Jürgen O Schumacher. Continuum modelling and simulation of flow batteries. *Flow Batteries: From Fundamentals to Applications*, 1:379–412, 2023.
- [14] Dongjiang You, Huamin Zhang, and Jian Chen. A simple model for the vanadium redox battery. *Electrochimica Acta*, 54(27):6827–6836, 2009.
- [15] Deepak Krishnamurthy, Erik O Johansson, Jin Wook Lee, and Erik Kjeang. Computational modeling of microfluidic fuel cells with flow-through porous electrodes. *Journal of Power Sources*, 196(23):10019–10031, 2011.
- [16] IM Bayanov and R Vanhaelst. The numerical simulation of vanadium redox flow batteries. *Journal of mathematical chemistry*, 49:2013–2031, 2011.

- [17] Edmund JF Dickinson and Andrew J Wain. The butler-volmer equation in electrochemical theory: Origins, value, and practical application. *Journal of Electroanalytical Chemistry*, 872:114145, 2020.
- [18] Piergiorgio Alotto, Massimo Guarnieri, and Federico Moro. Redox flow batteries for the storage of renewable energy: A review. *Renewable and sustainable energy reviews*, 29:325–335, 2014.
- [19] Grigory I Barenblatt, Iu P Zheltov, and IN Kochina. Basic concepts in the theory of seepage of homogeneous liquids in fissured rocks [strata]. *Journal of applied mathematics and mechanics*, 24(5):1286–1303, 1960.
- [20] Yuhe Wang and Yating Wang. Physical similarity of fluid flow in bimodal porous media: Part 1–basic model and solution characteristics. *arXiv preprint arXiv:2408.16434*, 2024.
- [21] H H Gerke and M Th Van Genuchten. A dual-porosity model for simulating the preferential movement of water and solutes in structured porous media. *Water resources research*, 29(2):305–319, 1993.
- [22] Todd Arbogast. Computational aspects of dual-porosity models. In *Homogenization and porous media*, pages 203–223. Springer, 1997.
- [23] I Yucel Akkutlu, Yalchin Efendiev, Maria Vasilyeva, and Yuhe Wang. Multiscale model reduction for shale gas transport in a coupled discrete fracture and dual-continuum porous media. *Journal of Natural Gas Science and Engineering*, 48:65–76, 2017.
- [24] Min Wang, Siu Wun Cheung, Eric T Chung, Maria Vasilyeva, and Yuhe Wang. Generalized multiscale multicontinuum model for fractured vuggy carbonate reservoirs. *Journal of Computational and Applied Mathematics*, 366:112370, 2020.
- [25] Tomas Vogel, Jan Brezina, Michal Dohnal, and Jaromir Dusek. Physical and numerical coupling in dual-continuum modeling of preferential flow. *Vadose Zone Journal*, 9(2):260–267, 2010.
- [26] Rolando Guidelli, Richard G Compton, Juan M Feliu, Eliezer Gileadi, Jacek Lipkowski, Wolfgang Schmickler, and Sergio Trasatti. Defining the transfer coefficient in electrochemistry: An assessment (iupac technical report). *Pure and Applied Chemistry*, 86(2):245–258, 2014.
- [27] Wolfgang Dreyer, Clemens Gohlke, and Rüdiger Müller. A new perspective on the electron transfer: recovering the butler–volmer equation in non-equilibrium thermodynamics. *Physical Chemistry Chemical Physics*, 18(36):24966–24983, 2016.
- [28] J Raphael Seidenberg, Alexander Mitsos, and Dominik Bongartz. Interpreting concentration and activation overpotentials in electrochemical systems: A critical discussion. *Journal of The Electrochemical Society*, 172(4):043506, 2025.
- [29] Qian Xu and TS Zhao. Fundamental models for flow batteries. *Progress in Energy and Combustion Science*, 49:40–58, 2015.
- [30] Yasser Ashraf Gandomi, DS Aaron, TA Zawodzinski, and MM Mench. In situ potential distribution measurement and validated model for all-vanadium redox flow battery. *Journal of The Electrochemical Society*, 163(1):A5188, 2015.

- [31] Yunxiang Chen, Jie Bao, Zhijie Xu, Peiyuan Gao, Litao Yan, Soowhan Kim, and Wei Wang. A hybrid analytical and numerical model for cross-over and performance decay in a unit cell vanadium redox flow battery. *Journal of Power Sources*, 578:233210, 2023.
- [32] Akeel A Shah, MJ Watt-Smith, and FC Walsh. A dynamic performance model for redox-flow batteries involving soluble species. *Electrochimica Acta*, 53(27):8087–8100, 2008.
- [33] Joseba Martinez Lopez, Iñigo Aramendia, Unai Fernandez-Gamiz, Eduardo Sanchez-Diez, Aitor Beloki, Erol Kurt, and Jose Manuel Lopez-Guede. Computational modeling of a 2d vanadium redox flow battery cell. *JOM*, 76(1):130–140, 2024.
- [34] Rudolph A Marcus. Electron transfer reactions in chemistry theory and experiment. *Journal of Electroanalytical Chemistry*, 438(1-2):251–259, 1997.
- [35] Tulong Zhu and SN1633725 Atluri. A modified collocation method and a penalty formulation for enforcing the essential boundary conditions in the element free galerkin method. *Computational Mechanics*, 21(3):211–222, 1998.
- [36] Alfio Quarteroni and Alberto Valli. *Numerical approximation of partial differential equations*. Springer, 1994.
- [37] J Frédéric Bonnans, J Charles Gilbert, Claude Lemaréchal, and Claudia A Sagastizábal. *Numerical optimization: theoretical and practical aspects*. Springer, 2006.
- [38] Adi Ben-Israel and Thomas NE Greville. *Generalized inverses: theory and applications*. Springer, 2003.
- [39] Gene H Golub and Charles F Van Loan. *Matrix computations*. JHU press, 2013.
- [40] Gene H Golub, Per Christian Hansen, and Dianne P O’Leary. Tikhonov regularization and total least squares. *SIAM journal on matrix analysis and applications*, 21(1):185–194, 1999.
- [41] João Carlos Alves Barata and Mahir Saleh Hussein. The moore–penrose pseudoinverse: A tutorial review of the theory. *Brazilian Journal of Physics*, 42:146–165, 2012.
- [42] Christopher C Paige and Michael A Saunders. Solution of sparse indefinite systems of linear equations. *SIAM journal on numerical analysis*, 12(4):617–629, 1975.
- [43] David Chin-Lung Fong and Michael Saunders. Lsmr: An iterative algorithm for sparse least-squares problems. *SIAM Journal on Scientific Computing*, 33(5):2950–2971, 2011.
- [44] Christopher C Paige and Michael A Saunders. Lsqr: An algorithm for sparse linear equations and sparse least squares. *ACM Transactions on Mathematical Software (TOMS)*, 8(1):43–71, 1982.
- [45] Arindam Ghosh and Sarit Maitra. The first integral method and some nonlinear models. *Computational and Applied Mathematics*, 40(3):79, 2021.
- [46] Uri M Ascher, Robert MM Mattheij, and Robert D Russell. *Numerical solution of boundary value problems for ordinary differential equations*. SIAM, 1995.
- [47] William H Press. *Numerical recipes 3rd edition: The art of scientific computing*. Cambridge university press, 2007.

Supplementary Information

A Solution Uniqueness of Galvanostatic Solution

We prove that the following system admits a unique set of solution pairs (ϕ_e, ϕ_l) up to an additive constant:

$$\nabla \cdot (-\sigma \nabla \phi_e) = -f(\eta) \quad \text{in } \Omega_e, \quad (\text{A.1a})$$

$$\nabla \cdot (-\kappa \nabla \phi_l) = f(\eta) \quad \text{in } \Omega_l, \quad (\text{A.1b})$$

$$\sigma \frac{\partial \phi_e}{\partial n} = g_e \quad \text{on } \partial\Omega_e, \quad (\text{A.1c})$$

$$\kappa \frac{\partial \phi_l}{\partial n} = g_l \quad \text{on } \partial\Omega_l. \quad (\text{A.1d})$$

where $f = a \sinh(b\eta)$ and $\eta = \phi_e - \phi_l - E_{eq}$.

Let (ϕ_e^1, ϕ_l^1) and (ϕ_e^2, ϕ_l^2) be two pairs of solutions to (A.1a)–(A.1d). We subtract (A.1a) and (A.1b) for $\phi_{e/l}^2$ from those equations for $\phi_{e/l}^1$ and define $\xi_e := \phi_e^1 - \phi_e^2$, $\xi_l := \phi_l^1 - \phi_l^2$, $\eta^1 := \phi_e^1 - \phi_l^1 - E_{eq}$, and $\eta^2 := \phi_e^2 - \phi_l^2 - E_{eq}$. They satisfy the following equations:

$$\nabla \cdot (-\sigma \nabla \xi_e) = -f(\eta^1) + f(\eta^2),$$

$$\nabla \cdot (-\kappa \nabla \xi_l) = f(\eta^1) - f(\eta^2).$$

Here, the subscripts (e/l) refer to the electrode and electrolyte, respectively, while the superscripts (1/2) denote the first and second pairs of solutions.

We then multiply both equations by (ξ_e, ξ_l) respectively and perform integration over $\Omega_{e/l}$, we have:

$$\int_{\Omega_e} \xi_e \nabla \cdot (-\sigma \nabla \xi_e) dx = - \int_{\Omega_e} \xi_e [f(\eta^1) - f(\eta^2)] dx, \quad (\text{A.2a})$$

$$\int_{\Omega_l} \xi_l \nabla \cdot (-\kappa \nabla \xi_l) dx = \int_{\Omega_l} \xi_l [f(\eta^1) - f(\eta^2)] dx. \quad (\text{A.2b})$$

We process the integral terms on the left-hand side by integration by parts and we can arrive at:

$$\int_{\Omega_e} \xi_e \nabla \cdot (-\sigma \nabla \xi_e) dx = \int_{\Omega_e} \sigma |\nabla \xi_e|^2 dx - \int_{\partial\Omega_e} \xi_e \sigma \frac{\partial \xi_e}{\partial n} dS_e,$$

$$\int_{\Omega_l} \xi_l \nabla \cdot (-\kappa \nabla \xi_l) dx = \int_{\Omega_l} \kappa |\nabla \xi_l|^2 dx - \int_{\partial\Omega_l} \xi_l \kappa \frac{\partial \xi_l}{\partial n} dS_l,$$

Since $\xi_e := \phi_e^1 - \phi_e^2$, $\xi_l := \phi_l^1 - \phi_l^2$, we know $\sigma \frac{\partial \xi_e}{\partial n} = 0$ on $\partial\Omega_e$ and $\kappa \frac{\partial \xi_l}{\partial n} = 0$ on $\partial\Omega_l$. And thus,

$$\int_{\Omega_e} \sigma |\nabla \xi_e|^2 dx = - \int_{\Omega_e} \xi_e [f(\eta^1) - f(\eta^2)] dx, \quad (\text{A.4a})$$

$$\int_{\Omega_l} \kappa |\nabla \xi_l|^2 dx = \int_{\Omega_l} \xi_l [f(\eta^1) - f(\eta^2)] dx. \quad (\text{A.4b})$$

By summing (A.4a) and (A.4b) together, we obtain:

$$\begin{aligned} 0 &\leq \int_{\Omega_e} \sigma |\nabla \xi_e|^2 + \int_{\Omega_l} \kappa |\nabla \xi_l|^2 = - \int_{\Omega} [f(\eta^1) - f(\eta^2)](\xi_e - \xi_l) dx \\ &= - \int_{\Omega} [f(\eta^1) - f(\eta^2)](\eta^1 - \eta^2) dx. \end{aligned} \quad (\text{A.5})$$

Noticing that

$$f'(\eta) = ab \cosh(b\eta) > 0,$$

we conclude that $f(\eta)$ is a strictly monotonically increasing function of η . This implies that for any given x ,

$$\text{if } \eta^1(x) > \eta^2(x) \implies f(\eta^1(x)) > f(\eta^2(x)),$$

$$\text{if } \eta^1(x) < \eta^2(x) \implies f(\eta^1(x)) < f(\eta^2(x)),$$

\Downarrow

$$\left[f(\eta^1(x)) - f(\eta^2(x)) \right] (\eta^1(x) - \eta^2(x)) \geq 0, \quad \forall x \in \Omega.$$

Integrating over the entire domain, we obtain

$$- \int_{\Omega} [f(\eta^1) - f(\eta^2)](\eta^1 - \eta^2) dx \leq 0.$$

Since the integral is non-negative, the only possibility for equality to hold is when the integrand itself is zero almost everywhere in Ω , leading to

$$f(\eta^1) - f(\eta^2) = 0 \quad \text{a.e. in } \Omega. \quad (\text{A.6})$$

Since $f(\eta)$ is strictly monotonic, this directly implies that

$$\eta^1(x) = \eta^2(x) \quad \text{a.e. in } \Omega.$$

Recalling that $\eta = \phi_e - \phi_l - E_{\text{eq}}$, we immediately obtain

$$\xi_e(x) = \xi_l(x) \quad \text{a.e. in } \Omega.$$

Now, looking back at (A.5), we notice

$$\int_{\Omega} \sigma |\nabla \xi_e|^2 dx + \int_{\Omega} \kappa |\nabla \xi_l|^2 dx = 0,$$

we conclude that

$$\nabla \xi_e = 0, \quad \nabla \xi_l = 0 \quad \text{a.e. in } \Omega.$$

This implies that both ξ_e and ξ_l must be spatially constant in Ω , i.e.,

$$\xi_e(x) = \xi_l(x) = C, \quad \text{a.e. in } \Omega$$

for some constant $C \in \mathbb{R}$.

Thus, any solution pair (ϕ_e, ϕ_l) to the system must be of the form:

$$\{(\phi_e, \phi_l) \mid \phi_e = \phi_e^* + C, \quad \phi_l = \phi_l^* + C, \quad C \in \mathbb{R}\}.$$

where the asterisk (*) denotes a particular pair of solutions. That is, ϕ_e^* and ϕ_l^* represent a specific set of solutions to the system, and any other solutions can be obtained by adding a constant C .

This completes the proof that the solution pair to the coupled nonlinear Neumann Poisson system is unique up to an additive constant C .

B Dirichlet's Principle and Lagrange Multiplier

We consider here a coupled Poisson system under all-Neumann boundary conditions in the following general form:

$$\nabla \cdot (-\sigma \nabla \phi_1) = -f(\phi_1 - \phi_2) \quad \text{in } \Omega, \quad (\text{B.1a})$$

$$\nabla \cdot (-\kappa \nabla \phi_2) = f(\phi_1 - \phi_2) \quad \text{in } \Omega, \quad (\text{B.1b})$$

$$\sigma \frac{\partial \phi_1}{\partial n} = g_1 \quad \text{on } \partial\Omega, \quad (\text{B.1c})$$

$$\kappa \frac{\partial \phi_2}{\partial n} = g_2 \quad \text{on } \partial\Omega. \quad (\text{B.1d})$$

where $f(\phi_1 - \phi_2) = a \sinh[b(\phi_1 - \phi_2 - E_{eq})]$, and a and b are some constants.

Based on Dirichlet's principle, We try to write a unified energy functional for this system as

$$\mathcal{E}(\phi_1, \phi_2) = \frac{1}{2} \int_{\Omega} \sigma |\nabla \phi_1|^2 + \frac{1}{2} \int_{\Omega} \kappa |\nabla \phi_2|^2 - \int_{\Omega} V(\phi_1, \phi_2) - \int_{\partial\Omega} g_1 \phi_1 - \int_{\partial\Omega} g_2 \phi_2 \quad (\text{B.2})$$

where:

- $\frac{1}{2} \int_{\Omega} \sigma |\nabla \phi_1|^2$ and $\frac{1}{2} \int_{\Omega} \kappa |\nabla \phi_2|^2$ represents the respective energy associated with the gradients of ϕ_1 and ϕ_2 , penalizing variations in ϕ_1 and ϕ_2 within Ω ;
- $V(\phi_1, \phi_2)$ is a potential energy term accounting for the interaction between the source/sink term $(-f, f)$ and (ϕ_1, ϕ_2) within Ω ;
- $\int_{\partial\Omega} g_1 \phi_1$ and $\int_{\partial\Omega} g_2 \phi_2$ incorporates the contributions of the Neumann boundary fluxes g_1 and g_2 to the energy of the coupled system.

For $V(\phi_1, \phi_2)$, we have that its partial derivative with respect to ϕ_1 yields $-f(\phi_1 - \phi_2)$ and with respect to ϕ_2 yields $f(\phi_1 - \phi_2)$. In a matrix form, we can express as:

$$\begin{bmatrix} \frac{\partial V(\phi_1, \phi_2)}{\partial \phi_1} \\ \frac{\partial V(\phi_1, \phi_2)}{\partial \phi_2} \end{bmatrix} = \begin{bmatrix} -f(\phi_1 - \phi_2) \\ f(\phi_1 - \phi_2) \end{bmatrix}. \quad (\text{B.3})$$

Note: For the case of (3a)–(3b), a natural choice for such potential function is

$$V(\phi_e, \phi_l) = -\frac{a}{b} \cosh(b\eta) \quad (\text{B.4})$$

with $\eta = \phi_e - \phi_l - E_{eq}$.

Next, we perform variational analysis to (B.2) by introducing a small perturbation to ϕ_1 such that:

$$\phi_1^{\epsilon_1} = \phi_1 + \epsilon_1 v_1, \quad (\text{B.5})$$

where ϵ_1 is an arbitrary small variable, and v_1 is an arbitrary smooth function.

Plug (B.5) in, we have:

$$\begin{aligned} \mathcal{E}(\phi_1^{\epsilon_1}, \phi_2) &= \frac{1}{2} \int_{\Omega} \sigma |\nabla(\phi_1 + \epsilon_1 v_1)|^2 + \frac{1}{2} \int_{\Omega} \kappa |\nabla \phi_2|^2 - \int_{\Omega} V[(\phi_1 + \epsilon_1 v_1), \phi_2] \\ &\quad - \int_{\partial\Omega} g_1(\phi_1 + \epsilon_1 v_1) - \int_{\partial\Omega} g_2 \phi_2 \end{aligned} \quad (\text{B.6})$$

Here $|\nabla(\phi_1 + \epsilon_1 v_1)|^2 = |\nabla \phi_1|^2 + 2\epsilon_1 \nabla \phi_1 \cdot \nabla v_1 + \epsilon_1^2 |\nabla v_1|^2$.

Differentiate (B.6) with respect to ϵ_1 and evaluate at $\epsilon_1 = 0$, then:

$$\left. \frac{\partial}{\partial \epsilon_1} \left(\frac{1}{2} \int_{\Omega} \sigma |\nabla(\phi_1 + \epsilon_1 v_1)|^2 \right) \right|_{\epsilon_1=0} = \int_{\Omega} \sigma \nabla \phi_1 \cdot \nabla v_1 \quad (\text{B.7a})$$

$$= \int_{\Omega} \nabla \cdot (-\sigma \nabla \phi_1) v_1 + \int_{\partial\Omega} \sigma \frac{\partial \phi_1}{\partial n} v_1, \quad (\text{B.7b})$$

$$\left. \frac{\partial}{\partial \epsilon_1} \left(\int_{\Omega} V[(\phi_1 + \epsilon_1 v_1), \phi_2] \right) \right|_{\epsilon_1=0} = \int_{\Omega} -f(\phi_1 - \phi_2) v_1, \quad (\text{B.7c})$$

$$\left. \frac{\partial}{\partial \epsilon_1} \left(\int_{\partial\Omega} g_1(\phi_1 + \epsilon_1 v_1) \right) \right|_{\epsilon_1=0} = \int_{\partial\Omega} g_1 v_1. \quad (\text{B.7d})$$

Similarly, if we perform the variation with respect to ϕ_2 , we have:

$$\left. \frac{\partial}{\partial \epsilon_2} \left(\frac{1}{2} \int_{\Omega} \kappa |\nabla(\phi_2 + \epsilon_2 v_2)|^2 \right) \right|_{\epsilon_2=0} = \int_{\Omega} \kappa \nabla \phi_2 \cdot \nabla v_2 \quad (\text{B.8a})$$

$$= \int_{\Omega} \nabla \cdot (-\kappa \nabla \phi_2) v_2 + \int_{\partial\Omega} \kappa \frac{\partial \phi_2}{\partial n} v_2, \quad (\text{B.8b})$$

$$\left. \frac{\partial}{\partial \epsilon_2} \left(\int_{\Omega} V[\phi_1, (\phi_2 + \epsilon_2 v_2)] \right) \right|_{\epsilon_2=0} = \int_{\Omega} f(\phi_1 - \phi_2) v_2, \quad (\text{B.8c})$$

$$\left. \frac{\partial}{\partial \epsilon_2} \left(\int_{\partial\Omega} g_2(\phi_2 + \epsilon_2 v_2) \right) \right|_{\epsilon_2=0} = \int_{\partial\Omega} g_2 v_2. \quad (\text{B.8d})$$

Thus, we have:

$$\left. \frac{\partial \mathcal{E}(\phi_1^{\epsilon_1}, \phi_2^{\epsilon_2})}{\partial(\epsilon_1, \epsilon_2)} \right|_{\epsilon_1=0, \epsilon_2=0} = \left[\begin{aligned} &\int_{\Omega} \nabla \cdot (-\sigma \nabla \phi_1) v_1 + \int_{\Omega} f(\phi_1 - \phi_2) v_1 - \int_{\partial\Omega} (g_1 - \sigma \frac{\partial \phi_1}{\partial n}) v_1 \\ &\int_{\Omega} \nabla \cdot (-\kappa \nabla \phi_2) v_2 - \int_{\Omega} f(\phi_1 - \phi_2) v_2 - \int_{\partial\Omega} (g_2 - \kappa \frac{\partial \phi_2}{\partial n}) v_2 \end{aligned} \right] \quad (\text{B.9})$$

To minimize the energy functional $\mathcal{E}(\phi_1, \phi_2)$, we set (B.9) to zero such that:

$$\left. \frac{\partial \mathcal{E}(\phi_1^{\epsilon_1}, \phi_2^{\epsilon_2})}{\partial(\epsilon_1, \epsilon_2)} \right|_{\epsilon_1=0, \epsilon_2=0} = \begin{bmatrix} 0 \\ 0 \end{bmatrix} \quad (\text{B.10})$$

Since v_1 and v_2 are arbitrary, (B.10) hold if and only if:

$$\nabla \cdot (-\sigma \nabla \phi_1) = -f(\phi_1 - \phi_2) \quad \text{in } \Omega, \quad (\text{B.11a})$$

$$\nabla \cdot (-\kappa \nabla \phi_2) = f(\phi_1 - \phi_2) \quad \text{in } \Omega, \quad (\text{B.11b})$$

$$\sigma \frac{\partial \phi_1}{\partial n} = g_1 \quad \text{on } \partial\Omega, \quad (\text{B.11c})$$

$$\kappa \frac{\partial \phi_2}{\partial n} = g_2 \quad \text{on } \partial\Omega. \quad (\text{B.11d})$$

We can see that the above obtained Euler–Lagrange equations exactly recover (B.1a)–(B.1b), and honor the original Neumann boundary conditions as in (B.1c)–(B.1d). By constructing a unified energy functional in this manner, even when the coefficients σ and κ differ, the variational formulation recovers the original coupled system in its entirety.

Remark: If the nonlinear term lacks antisymmetry, then no potential function $V(\phi_1, \phi_2)$ can reproduce (B.3), provided the reaction current density depends on $\phi_1 - \phi_2$. In other words, the system cannot be derived from a single unified energy functional when the coefficients of the nonlinear terms in the two equations are not balanced. This violates the principle of “conservativity” or “self-adjointness.” Consequently, if such coupled system is governed by an asymmetric nonlinear source/sink term, it is inherently impossible to construct a single energy functional to describe it.

Now, based on the unified energy functional (B.2), let us add some local Lagrange constraints to the coupled system. Suppose we want to impose constraints on ϕ_1 at certain specified positions Γ_1 within Ω , expressed as

$$\phi_1|_{\Gamma_1} = \vec{C}_1 \quad \text{at } \Gamma_1. \quad (\text{B.12})$$

We can use the Lagrange multiplier method to introduce a set of multipliers λ_i (which are additional global unknowns but only act at the “constraint point”), and construct the following augmented energy functional:

$$\mathcal{L}(\phi_1, \phi_2, \lambda) = \mathcal{E}(\phi_1, \phi_2) + \sum_{i=1}^m \lambda_i [\phi_1(x_i) - c_i] \quad (\text{B.13})$$

$x_i \in \Omega$ are the discrete points to enforce constraint, given by the set $\Gamma_1 := \{x_1, x_2, \dots, x_m\}$.

To derive the extended Euler-Lagrange equations of (B.13), we take variation of \mathcal{L} with respect to ϕ_1 , ϕ_2 , and λ . Utilizing the respective Euler-Lagrange equations of $\mathcal{E}(u_1, u_2)$, we can obtain the following extended Lagrange system:

$$\nabla \cdot (-\sigma \nabla \phi_1) + f + \sum_{i=1}^m \lambda_i \delta(x - x_i) = 0 \quad \text{in } \Omega \quad (\text{B.14a})$$

$$\nabla \cdot (-\kappa \nabla \phi_2) - f = 0 \quad \text{in } \Omega \quad (\text{B.14b})$$

$$\phi_1(x_i) - c_i = 0 \quad \text{for } x_i \in \Gamma_1 \quad (\text{B.14c})$$

with Neumann conditions given in (B.1c)–(B.1d).

Here, $\delta(x - x_i)$ is Dirac delta function, meaning λ_i effects the system only at x_i .

C Line Search Method for Reference Potential Matching

To refine the reference potential c_l for the electrolyte domain, we employ a gradient descent-based line search methods within an optimization framework. This iterative approach aims to minimize the objective function J , as defined in (18), ensuring that the solution adheres to charge conservation. Gradient descent updates the reference potential by moving in the direction of the negative gradient of the objective function. The gradient is computed using a finite-difference approximation:

$$\nabla J(c_l) \approx \frac{J(c_l + \delta) - J(c_l)}{\delta} \quad (\text{C.1})$$

Alternatively, central finite differences can be used for higher accuracy, given by:

$$\nabla J(c_l) \approx \frac{J(c_l + \delta) - J(c_l - \delta)}{2\delta} \quad (\text{C.2})$$

where δ is a small perturbation. The iterative update rule is:

$$c_l^{(k+1)} = c_l^{(k)} - \beta \nabla J(c_l^{(k)}) \quad (\text{C.3})$$

where $\beta > 0$ is the step size. To ensure convergence, the step size is adjusted using the Armijo condition:

$$J(c_l^{(k+1)}) \leq J(c_l^{(k)}) + c\beta \nabla J(c_l^{(k)}) (-\nabla J(c_l^{(k)})) \quad (\text{C.4})$$

where $c \in (0, 1)$ is a small constant, and β is initialized to a default value and iteratively adjusted as follows: 1. Start with an initial $\beta > 0$. 2. Reduce β by a factor of $\rho \in (0, 1)$ (e.g., $\rho = 0.5$) until the Armijo condition is met. 3. Use the updated β for the next iteration.

D Exact Solution Expression (27)

We use the First Integral Method to find the exact solution of (27) in 1D under galvanostatic and potentiostatic conditions.

Step 1: First Integral

The given PDE is:

$$\frac{d^2\eta}{dx^2} = a' \sinh(b\eta). \quad (\text{D.1})$$

Multiply both sides by $\frac{d\eta}{dx}$ to prepare for integration:

$$\frac{d^2\eta}{dx^2} \frac{d\eta}{dx} = a' \sinh(b\eta) \frac{d\eta}{dx} \quad (\text{D.2})$$

Rewriting the left-hand side as a total derivative:

$$\frac{d}{dx} \left(\frac{1}{2} \left(\frac{d\eta}{dx} \right)^2 \right) = \frac{d}{dx} \left(\frac{a'}{b} \cosh(b\eta) \right) \quad (\text{D.3})$$

Integrate both sides once:

$$\frac{1}{2} \left(\frac{d\eta}{dx} \right)^2 = \frac{a'}{b} \cosh(b\eta) + C \quad (\text{D.4})$$

where C is the integration constant.

Then, we use the Neumann boundary conditions to determine C .

Step 2: Apply Boundary Conditions

At $x = 0$:

$$\frac{1}{2} q_1^2 = \frac{a'}{b} \cosh(b\eta_0) + C \quad (\text{D.5})$$

At $x = W$:

$$\frac{1}{2} q_2^2 = \frac{a'}{b} \cosh(b\eta_W) + C \quad (\text{D.6})$$

where $q_1 = \frac{d\eta}{dx}(0)$, $q_2 = \frac{d\eta}{dx}(W)$, $\eta_0 = \eta(0)$ and $\eta_W = \eta(W)$. We can use either boundary equation to find the expression for C , such that:

$$C = \frac{1}{2} q_1^2 - \frac{a'}{b} \cosh(b\eta_0) \quad (\text{D.7})$$

Step 3: Solve for x

Rearrange:

$$\frac{d\eta}{dx} = \sqrt{\frac{2a'}{b} \cosh(b\eta) + q_1^2 - \frac{2a'}{b} \cosh(b\eta_0)}. \quad (\text{D.8})$$

Separating variables:

$$dx = \frac{d\eta}{\sqrt{\frac{2a'}{b} \cosh(b\eta) + q_1^2 - \frac{2a'}{b} \cosh(b\eta_0)}}. \quad (\text{D.9})$$

Integrate:

$$x = \int_{\eta_0}^{\eta} \frac{d\eta}{\sqrt{\frac{2a'}{b} \cosh(b\eta) + q_1^2 - \frac{2a'}{b} \cosh(b\eta_0)}}. \quad (\text{D.10})$$

This defines an implicit relation between x and $\eta(x)$, which needs to be evaluated numerically as we end up with an integral problem. We can then apply numerical integration or approximate using elliptic functions.